

A New Look at the Large-Scale H I Structure of the LMC

L. Staveley-Smith,^{1*} S. Kim,² M. R. Calabretta,¹ R. F. Haynes,^{1,3}
and M. J. Kesteven¹

¹*Australia Telescope National Facility, CSIRO, P.O. Box 76, Epping, NSW 1710, Australia*

²*Harvard Smithsonian Center for Astrophysics, 60 Garden Street, Cambridge, MA 02138, U.S.A*

³*School of Mathematics and Physics, University of Tasmania, P.O. Box 252-37, Hobart, Tasmania 7001, Australia*

Accepted 2002 October 8. Received 2002 July 24

ABSTRACT

We present a Parkes multibeam H I survey of the Large Magellanic Cloud (LMC). This survey, which is sensitive to spatial structure in the range 200 pc \sim 10 kpc, complements the Australia Telescope Compact survey, which is sensitive to structure in the range 15 pc \sim 500 pc. With an rms column density sensitivity of 8×10^{16} cm⁻² for narrow lines and 4×10^{17} cm⁻² for typical linewidths of 40 km s⁻¹, emission is found to be extensive well beyond the main body of the LMC. Arm-like features extend from the LMC to join the Magellanic Bridge and the Leading Arm, a forward counterpart to the Magellanic Stream. These features, whilst not as dramatic as those in the SMC, appear to have a common origin in the Galactic tidal field, in agreement with recent 2MASS and DENIS results for the stellar population. The diffuse gas which surrounds the LMC, particularly at ℓ 's 90° to 330°, appears to be loosely associated with tidal features, but loosening by the ram pressure of tenuous Galactic halo gas against the outer parts of the LMC cannot be discounted. High-velocity clouds, which lie between the Galaxy and the LMC in velocity and which appear in the UV spectra of some LMC stars, are found to be associated with the LMC if their heliocentric velocity exceeds about +100 km s⁻¹. They are possibly the product of energetic outflows from the LMC disk. The H I mass of the LMC is found to be $(4.8 \pm 0.2) \times 10^8 M_{\odot}$ (for an assumed distance of 50 kpc), substantially more than previous recent measurements.

Key words: surveys – galaxies: LMC, Magellanic Clouds - radio lines: galaxies

1 INTRODUCTION

The LMC plays a key role in our understanding of diverse areas in astronomy, including the extragalactic distance scale which uses the LMC as a zero-point (Feast 1999, Gibson 1999), the formation of star clusters (Johnson et al. 1999) and H II regions (Oey 1996), molecular cloud astrophysics (Johansson et al. 1994), and for providing background stars with which to study possible microlenses in the Galactic halo (Alcock et al. 2000). With this in mind, Kim et al. (1998a) surveyed the LMC in H I at high spatial resolution with the Australia Telescope Compact Array (ATCA). This data has since served to help study the interaction between star-forming regions and the interstellar medium at small scales (e.g. Kim et al. 1998b; Kim et al. 1999; Points et al. 2000; Olsen, Kim & Buss 2001). However its use for large-scale studies (with notable exceptions, e.g. the study of the LMC disk and halo dynamics by Alves & Nelson 2000) is largely confined to morphological studies and comparisons

(e.g. Wada, Spaans & Kim 2000). The reason for this is that, being an interferometer, the ATCA is insensitive to structure on an angular size scale larger than λ/B , where the shortest baseline is $B = 30$ m (~ 20 m when the finite antenna size is taken into consideration and when the sky is Nyquist-sampled by the antenna primary beams). This corresponds to ~ 0.5 or about 0.4 kpc at the distance of the LMC (assumed here to be 50 kpc).

The missing large-scale structure means that H I column densities are difficult to derive. For example, accurate optical depths for X-ray photoelectric absorption cannot be obtained. It also makes it difficult to compare the H I structure of large shells against competing models of their formation, e.g. stellar winds (Dopita, Mathewson & Ford 1985), high-velocity cloud collisions (Braun 1996) and gamma-ray bursts (Efremov, Ehlerová & Palouš 1999). Similarly, the outer tidal structure of the LMC cannot be compared with the recent stellar results from 2MASS and DENIS (van der Marel 2001).

Observations sensitive to large spatial scales may be taken from the autocorrelations from the individual anten-

* email: Lister.Staveley-Smith@csiro.au

nas of an interferometer. But this data is often not calibrated in a suitable way. Moreover, for a homogeneous interferometer such as the ATCA, there exists a serious gap in the UV-plane between the auto and cross-correlation data. It is usually more useful to collect data from a large single-dish antenna such as the Parkes telescope[†] which, with a diameter of 64 m, is much larger than the smallest ATCA baseline. There are several excellent studies using Parkes of HI in the LMC, however none is particularly suitable for the present purpose. Needless to say, the older studies (McGee & Milton 1966) are not available digitally. The observations of Luks & Rohlf (1992) do not cover a sufficient spatial area (they cut off the LMC disk north of Dec. -66°) and are not Nyquist-sampled. The HIPASS observations (Putman et al. 2002) have insufficient velocity resolution and, since HIPASS was designed to detect compact extragalactic objects (Barnes et al. 2001), also impose a high-pass filter on the sky.

The task of mapping a large area such as the LMC at the Nyquist rate (5.7 for Parkes at $\lambda 21$ cm) is not straightforward as $\sim 10^4$ pointings are required. Fortunately, the advent of a 21 cm multibeam receiver at Parkes (Staveley-Smith et al. 1996) makes the task easier, so observations were undertaken following the installation of new narrow-band filters in late-1998. We describe the Parkes observations in Section 2 and discuss the general morphology, tidal features and spatially integrated properties in Section 3. We also compare our results with previous work. In Section 4, we discuss halo gas in the LMC, particularly in the sight-line from our Galaxy. In Section 5, we look again at the largest H I holes and associated high-velocity gas. Finally, in Section 6, we use the Galactic part of the velocity range to re-discuss foreground absorption. The combination of the existing data with the ATCA data is separately described in Kim et al. (2002), and some early results from the combined data set are discussed by Elmegreen, Kim & Staveley-Smith (2001) and Padoan et al. (2001).

2 OBSERVATIONS

Observations were taken with the inner seven beams of the Parkes 21 cm multibeam receiver (Staveley-Smith et al. 1996) on 1998 December 13 to 17. The telescope was scanned across the LMC in orthogonal great circles aligned approximately east-west and north-south. The receiver was continuously rotated such that the rotation angle was always at $19^\circ 1'$ to the scan trajectory, the appropriate angle in a hexagonal geometry for ensuring uniform spatial sampling of the sky. The area covered was 13° by 14° in RA and Dec, respectively, and centred on RA $05^h 20^m$, Dec. $-68^\circ 44'$ (J2000). This corresponds to 8–9 disk scale lengths in the optical or infrared (Bothun & Thompson 1988, van der Marel 2001). In a single scan, the spacing between adjacent tracks is $9'.5$, which is smaller than the mean FWHP beamwidth of $14'.1$, but greater than the Nyquist interval ($\lambda/2D$) of $5'.7$. Therefore, six scans were interleaved in each of the principal scan directions, resulting in a final track spacing of $1'.6$. In

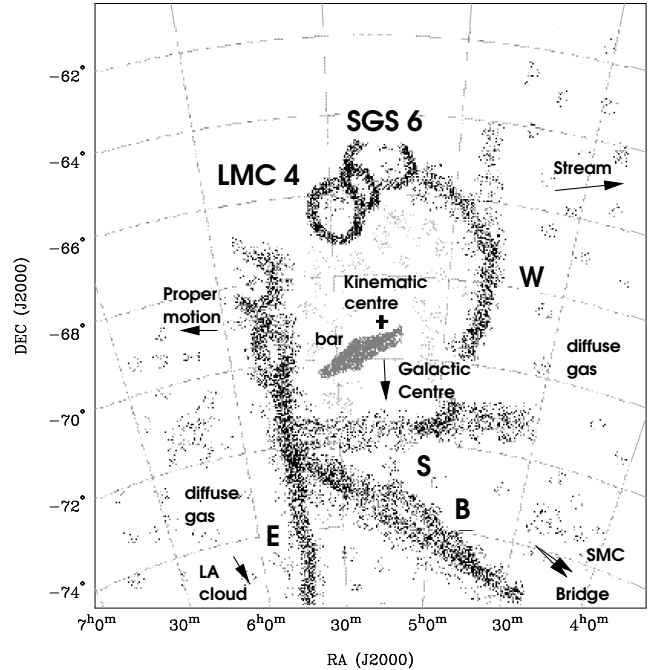


Figure 1. A schematic showing the main outer features of the LMC in H I. The kinematic centre of Kim et al. (1998a) and the optical bar are included for reference. Arms B, E, S and W are the outer arms referred to in the text; LMC 4 (Meaburn 1980) and LMC SGS 6 (Kim et al. 1999) are supergiant shells; diffuse gas appears in the south-east, south and west of the LMC. The directions to the Galactic Centre, the Magellanic Bridge, the SMC, the Leading Arm cloud at $\ell = 292^\circ 4$, $-30^\circ 2$ and the Magellanic Stream (a vector at constant Magellanic latitude -5° , Putman et al. 2002) are shown. Also shown is the proper motion vector of Kroupa & Bastian (1997).

total, 12×6 RA scans and 11×6 Dec. scans were made. Seven scans were dropped or edited out due to drive problems, leaving a total of 131 scans consisting of a total of 29 h of on-source integration on each of seven beams. The average integration time per beam area is 360 s (both polarisations).

The scan rate of the telescope was 1.0 min^{-1} and the correlator was read every 5 s. Therefore, the beam was slightly broadened in the scan direction to $14'.5$ (Barnes et al. 2001). After averaging orthogonal scans, the effective beamwidth reduces to $14'.3$. The central observing frequency was switched between 1417.5 and 1421.5 MHz, again every 5 s. This allowed the bandpass shape to be calibrated without spending any time off-source. A bandwidth of 8 MHz was used with 2048 spectral channels in each of two orthogonal linear polarisations. H I emission from the LMC (and the Galaxy) appeared within the band at both frequency settings. After bandpass calibration, the data from both settings were shifted to a common heliocentric reference frame. The velocity spacing of the multibeam data is 0.82 km s^{-1} , but the final cube was Hanning-smoothed to a resolution of 1.6 km s^{-1} . The useful velocity range in the final cube (i.e. after excluding frequency sidelobes of the LMC and the Galaxy, and band-edge effects) is -66 to 430 km s^{-1} .

Bandpass calibration, velocity shifting and preliminary spectral baseline fitting were all done using the AIPS++ LIVEDATA task. Baselines were adaptively fitted using poly-

[†] The Parkes telescope is part of the Australia Telescope which is funded by the Commonwealth of Australia for operation as a National Facility managed by CSIRO.

nomials of degree 8. Subsequently, the data were convolved onto a grid of $4'$ pixels using a Gaussian kernel with a FWHP of $8'.0$. This broadens the effective, scan-broadened, beamwidth of the inner seven beams from $14'.3$ to about $16'.4$. Residual spectral baselines were removed by fitting polynomials in the image domain (MIRIAD task CONTSUB).

The multibeam data were calibrated relative to a flux density for PKS B1934-638 of 14.9 Jy at the observing frequency. The brightness temperature conversion factor of 0.80 K Jy $^{-1}$ was established by an observation of S9 ($T_B = 85$ K, Williams 1973). On the same scale, we measured a brightness temperature for pointing 416 (Stanimirović et al. 1999) in the SMC (RA $00^{\text{h}}47^{\text{m}}52.6^{\text{s}}$, Dec. $-73^{\circ}02'19''.8$, J2000) of $T_B = 133$ K, compared with the 137 K measured by Stanimirović et al. The 3% difference is probably due to the different characteristics of the feeds used in the two observations, and residual uncertainties in absolute bandpass calibration. The rms noise in the line-free region of the cube is 27 mK, which is close to the theoretical value. This corresponds to a column density sensitivity of 8×10^{16} cm $^{-2}$ across 1.6 km s $^{-1}$, and 4×10^{17} cm $^{-2}$ for linewidths of 40 km s $^{-1}$, typical of those in the LMC.

3 RESULTS

3.1 Channel Maps

The area covered by the present observations is shown in Fig. 1 together with some prominent features, referred to later in the text. Relevant directions and proper motion vectors to the Galaxy and other parts of the Magellanic system are also plotted.

Channel maps, formed by averaging groups of six channels are shown in Fig. 2. Maps between heliocentric velocities of 185.9 and 359.0 km s $^{-1}$ are shown, spaced by $6 \times 0.82 = 4.92$ km s $^{-1}$. Although this velocity range covers the main body of H I emission in the LMC, the emission does extend in a continuous manner down to ~ 100 km s $^{-1}$ and up to ~ 425 km s $^{-1}$, but at faint levels (see Section 4). There appears to be a small, but clean separation between H I in the LMC and H I in the Galaxy which extends from ~ 90 km s $^{-1}$ through to ~ -50 km s $^{-1}$. The Galactic component, important for extinction and photoelectric absorption estimates, is discussed in Section 6.

The main feature in the channel maps between 186 and 211 km s $^{-1}$ is the arm (hereafter arm ‘B’) of the LMC noted before in the Parkes observations by McGee & Newton (1986), the ATCA observations of Kim et al. (1998a), and in the HIPASS map presented by Gardiner, Turfuss & Putman (1998). Arm B appears to be a tidal feature which directly connects the LMC with the Magellanic Bridge joining the LMC and SMC. We discuss this further in Section 3.4.

Between 220 and 240 km s $^{-1}$, the southern part of the main body of the LMC becomes visible. The main body appears bounded by another arm (hereafter arm ‘S’) curving from RA $05^{\text{h}}30^{\text{m}}$, Dec. $-71^{\circ}30'$ to RA $04^{\text{h}}20^{\text{m}}$, Dec. $-70^{\circ}00'$ (J2000), and by a ‘figure-of-eight’ structure associated with the supergiant shell LMC2 (Points et al. 2000) and the gas complexes to the south of 30 Doradus (Mochizuki et al. 1994; Blondiau et al. 1997) which run from RA $05^{\text{h}}41^{\text{m}}$, Dec. $-72^{\circ}00'$ to RA $05^{\text{h}}45^{\text{m}}$, Dec. $-69^{\circ}00'$ (J2000).

Between 260 and 280 km s $^{-1}$, the LMC begins to look remarkably like a barred spiral galaxy (e.g. NGC 1365). Two arms open out at approximately Dec. -69° , the one at RA $04^{\text{h}}45^{\text{m}}$ (hereafter arm ‘W’) extending north for 5° , and the one at RA $05^{\text{h}}40^{\text{m}}$ (hereafter arm ‘E’) extending south for 6° to at least the limit of the map. The two arms are connected by H I but not in a structure which looks like a bar, nor a structure which is similar in position or position angle to the optical bar. Arm E points directly towards the Leading Arm cloud at RA $05^{\text{h}}28^{\text{m}}$, $-80^{\circ}15'$ (J2000), $v_{LSR} = 323$ km s $^{-1}$ ($\ell = 292^{\circ}.4$, $-30^{\circ}.2$, $v_h = 333$ km s $^{-1}$) shown in Putman et al. (1998). This cloud lies 11° (10 kpc, in projection) south of the start of arm E, and 4° beyond the edge of the present map. Deep HIPASS data show a continuous connection between the Leading Arm and Arm E at velocities between 260 and 300 km s $^{-1}$, heliocentric. Throughout the velocity range from 260 and 280 km s $^{-1}$, arm B also remains visible, showing that this gas is very disturbed and has velocity extent of at least 100 km s $^{-1}$.

Above 300 km s $^{-1}$, the northern half of the main body of the LMC is visible, and is dominated by: (a) the supergiant shell LMC4 (Meaburn 1980, Domgörgen, Bomans & de Boer 1995); (b) the supergiant shell LMC SGS 6 (Kim et al. 1999); and (c) the linear arm E, discussed above.

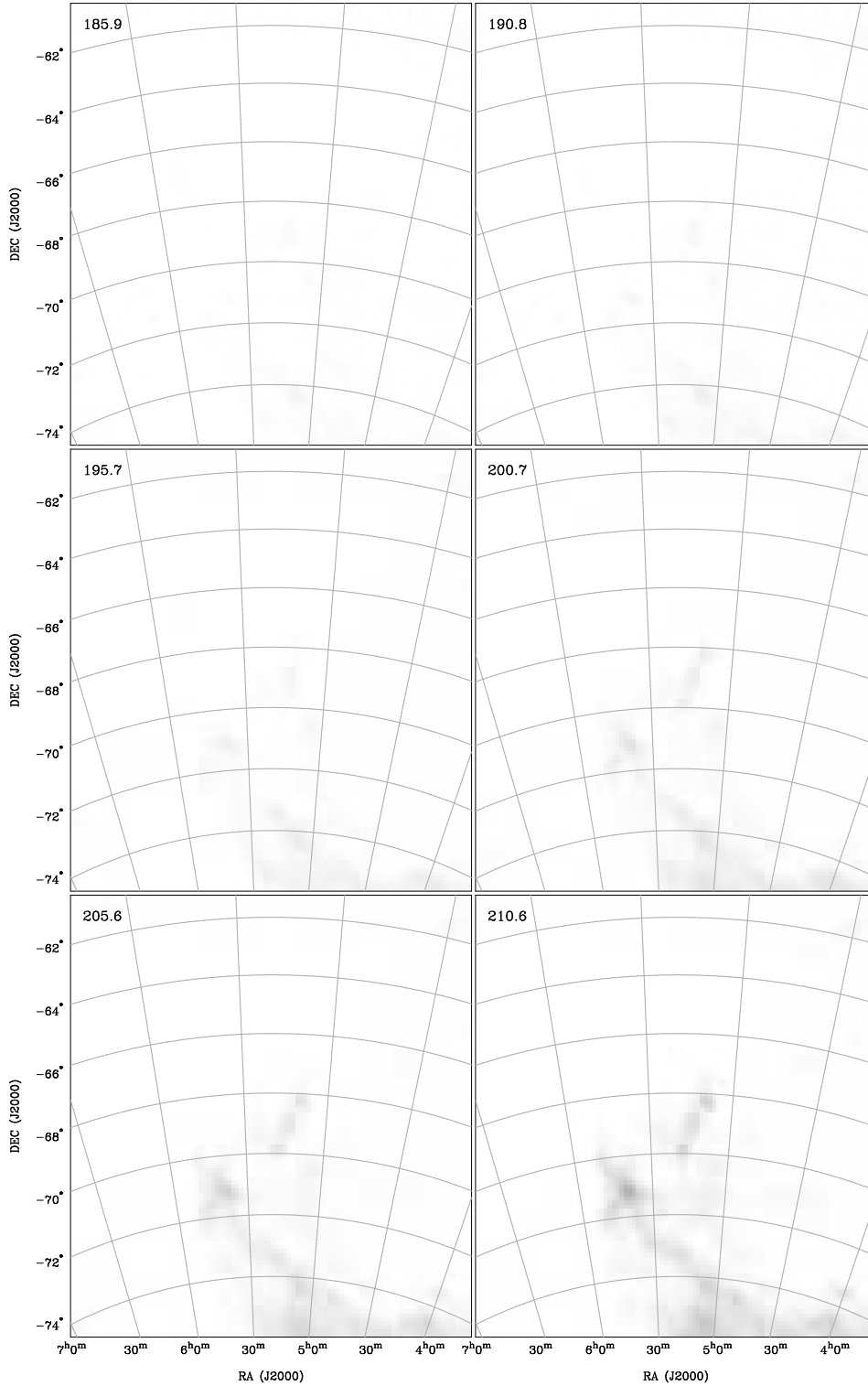


Figure 2. Channel maps of HI in the LMC formed by averaging six adjacent planes of the cube (for display purposes). The resultant velocity spacing is 4.92 km s^{-1} . The full intensity range 0 to 83.1 K is shown, with a square root transfer function. The heliocentric velocity of each velocity plane is shown at the top left in km s^{-1} .

3.2 Integrated H I Maps and the Morphology of the LMC

The peak brightness-temperature image and the column density image of the LMC are shown in Fig. 3. The peak

brightness temperature is 83.1 K at RA $05^{\text{h}}39^{\text{m}}22^{\text{s}}$, Dec. $-69^{\circ}51'13''$ (J2000), a position slightly south of N159 and the 30 Doradus H II complex. The peak column density of $5.6 \times 10^{21} \text{ cm}^{-2}$ lies at the same position. Both values are $\sim 50\%$ higher than the values in the Luks & Rohlfs (1992,

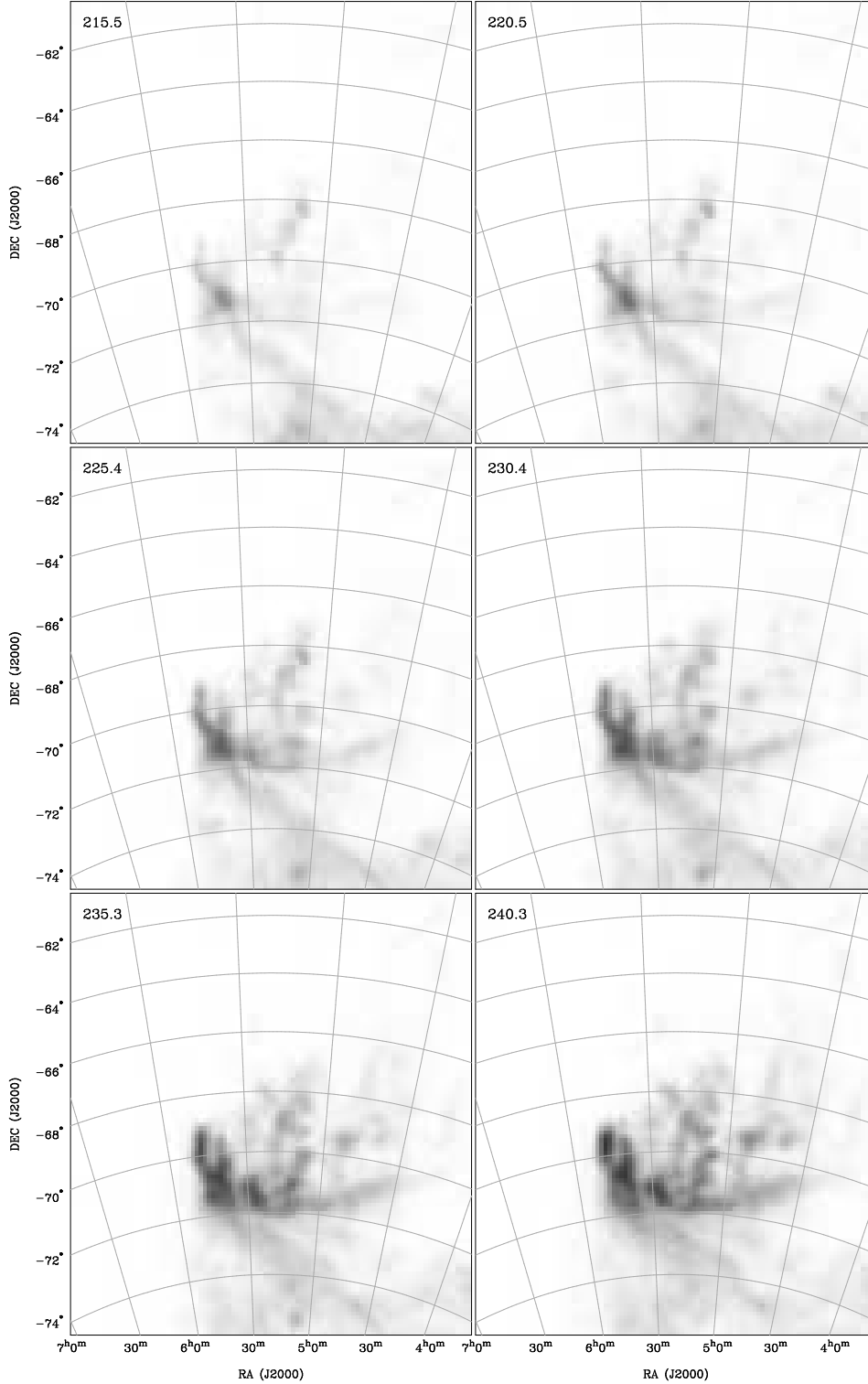
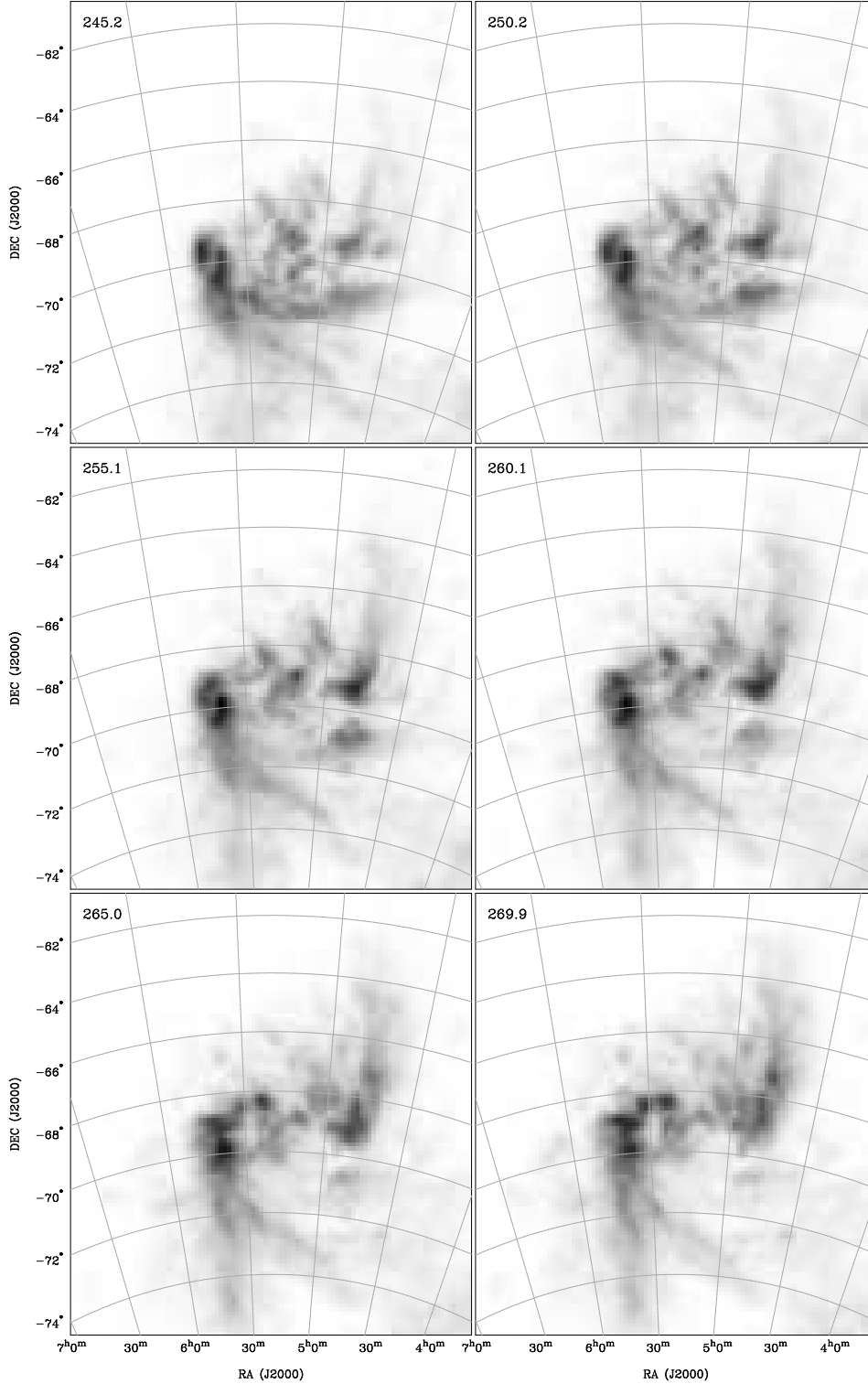


Figure 2 – continued

hereafter LR92) data (53 K and $3.6 \times 10^{21} \text{ cm}^{-2}$, respectively). Part of this difference is resolution. The present data were obtained with the multibeam receiver which has a mean beamwidth of $14'.1$, broadened to $16'.4$ after scanning and gridding effects are taken into account (Section 2). The LR92 data were taken with a feed with a beamwidth of $\sim 15'$ on

an undersampled grid of spacing $12'$ and interpolated onto a grid with similar spacing, presumably resulting in an effective resolution of $\gtrsim 20'$. However, there must also be a calibration difference as the HI mass measured here is ~ 30 per cent higher than that of LR92 (Section 3.3). A pixel-by-pixel comparison of the LR92 column densities and the column

**Figure 2** – *continued*

densities in this paper shows that this is the case (Fig. 4). The column density ratio is $N_{\text{HI}}/N_{\text{HI}}(\text{LR92}) = 1.43$. This sizeable calibration anomaly has been noted before (Blondiau et al. 1997 rescale LR92 temperatures by 1.5), and seriously affects use of LR92 column densities. As confirmed in Luks (1991), LR92 base their calibration on an earlier pa-

per (Rohlfs et al. 1984). This paper quotes column densities and temperatures based on antenna temperature, T_A rather than brightness temperature, T_B (their equation 5 and legend to Table 1). They further state that their HI column density “can be converted approximately into true column density by multiplication with $1/\eta_{mb} = 1.25$ ”. Assuming

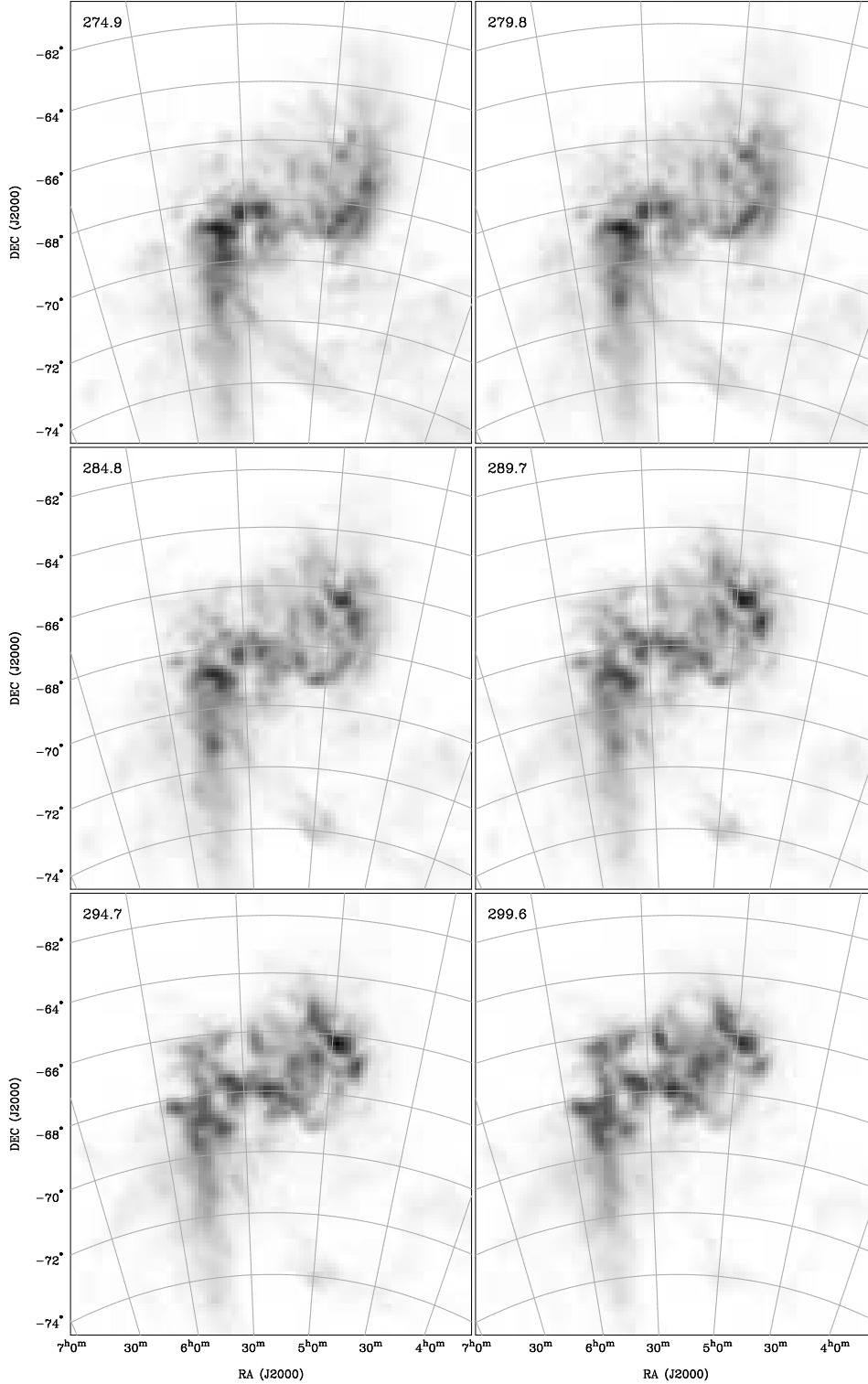
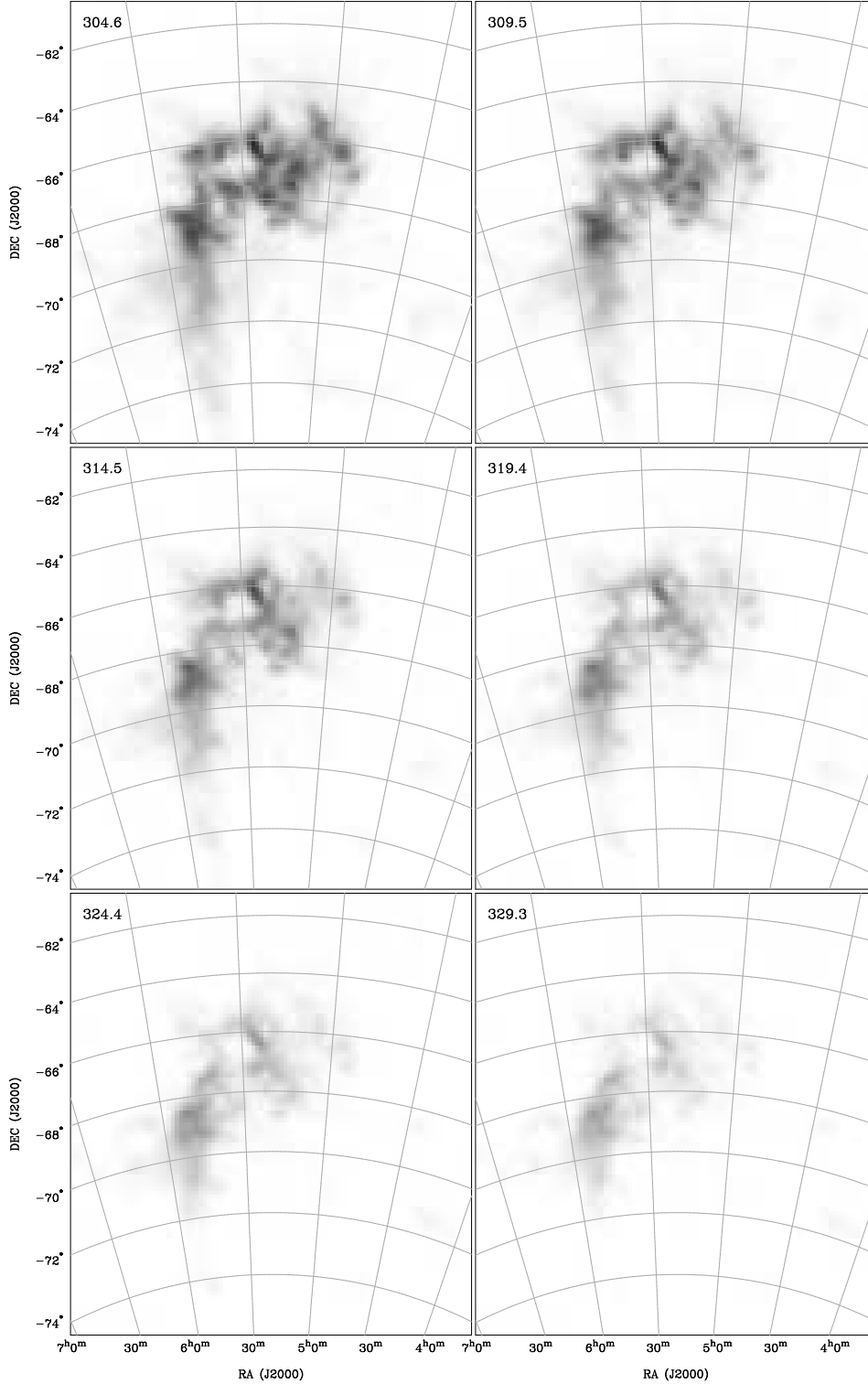


Figure 2 – continued

this factor has been neglected in LR92, the residual calibration difference then appears to be $1.43/1.25 = 1.14$. This may be explained by the high main beam efficiency (or low antenna efficiency) measured by Rohlfs et al. They measure a ratio $T_B/S_\nu = 0.775 \text{ K Jy}^{-1}$ for the Parkes telescope. In contrast, other measurements with the same single-beam,

hybrid-mode feed suggest $T_B/S_\nu = 0.85$ to 0.93 K Jy^{-1} (Davies, Staveley-Smith & Murray 1989, Stanimirović et al. 1999), a similar factor (1.12 ± 0.05) higher.

Our peak column density of $5.6 \times 10^{21} \text{ cm}^{-2}$ is also higher than that of McGee & Milton (1966) who quote $4.0 \times 10^{21} \text{ cm}^{-2}$. This is probably a resolution difference be-

**Figure 2** – *continued*

cause, as noted in Section 3.3, their total H I mass is virtually identical to ours. The ATCA data of Kim et al. (1998a) at 1' resolution show a higher peak brightness temperature of 106 K, increasing to a true value of 138 K when combined with the present multibeam data (Kim et al. 2002).

The main features of the H I distribution in Fig. 3 are:

- A well-defined, nearly circular disk forms the main body of the LMC, indicating a nearly face-on inclination if it is assumed that the LMC has an intrinsically circular disk. This agrees with other recent values based on this assumption (e.g. 22° – 26° Weinberg & Nikolaev 2001; $22 \pm 6^\circ$, Kim et al. 1998a), though not with values based in direct dis-

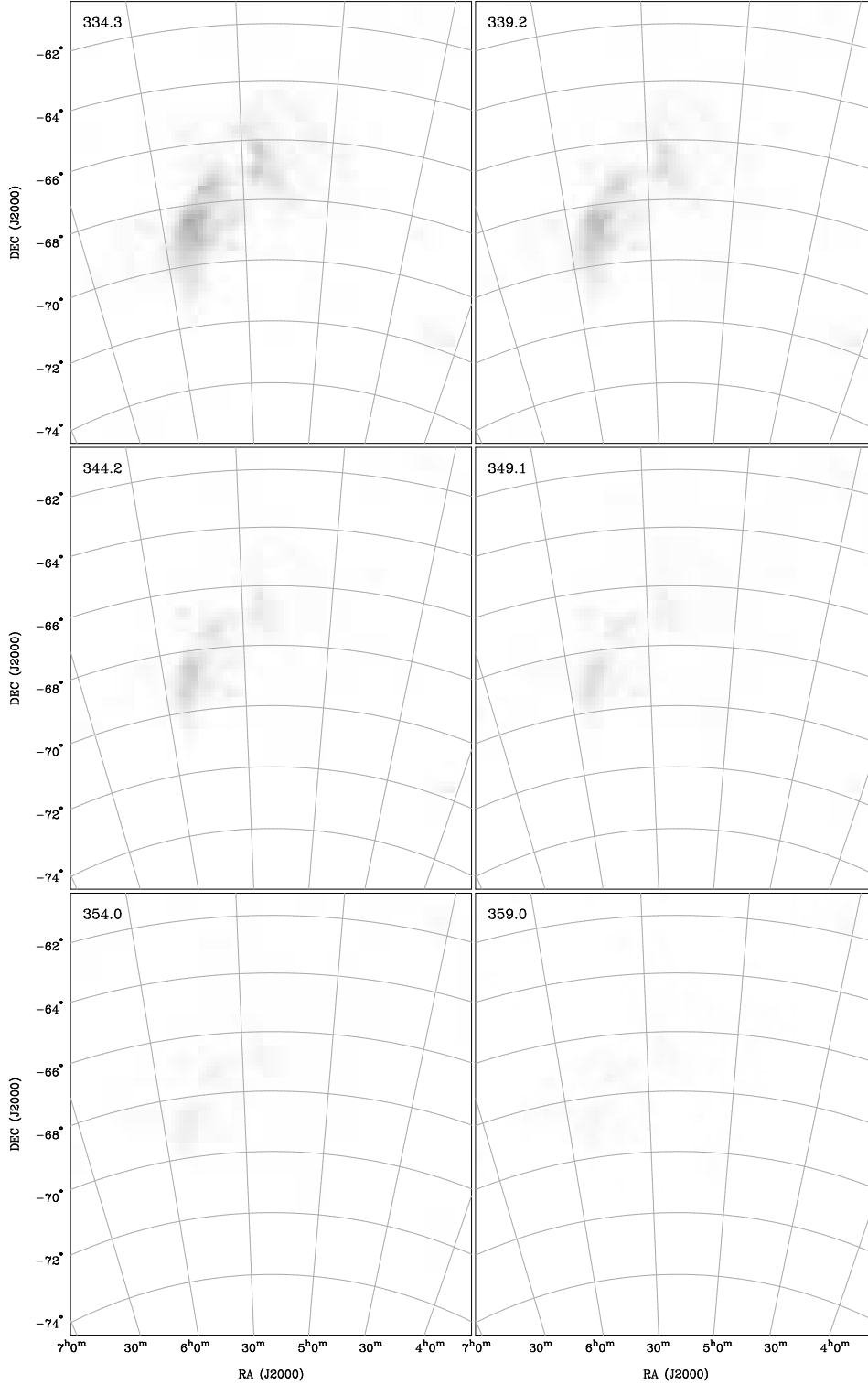


Figure 2 – continued

tance determination ($42^\circ \pm 7^\circ$, Weinberg & Nikolaev 2001; $35^\circ \pm 6^\circ$, van der Marel & Cioni 2001). The influence of tidal forces and non-circular motions in the outer parts of the disk doubtless contribute to this disagreement. van der Marel (2001) deduces an *intrinsic* ellipticity of 0.31 for the outer disk at near-infrared wavelengths. The bulk of the LMC H I

regions (Kennicutt et al. 1995, Kim et al. 1999) are contained within the gaseous disk.

- The body of the LMC is punctuated by large holes, and has a general mottled appearance. The main H I gaps are at RA $05^{\text{h}}32^{\text{m}}$, Dec. $-66^\circ45'$ (J2000), corresponding to LMC 4 (Meaburn 1980) and, in the column density image, the large

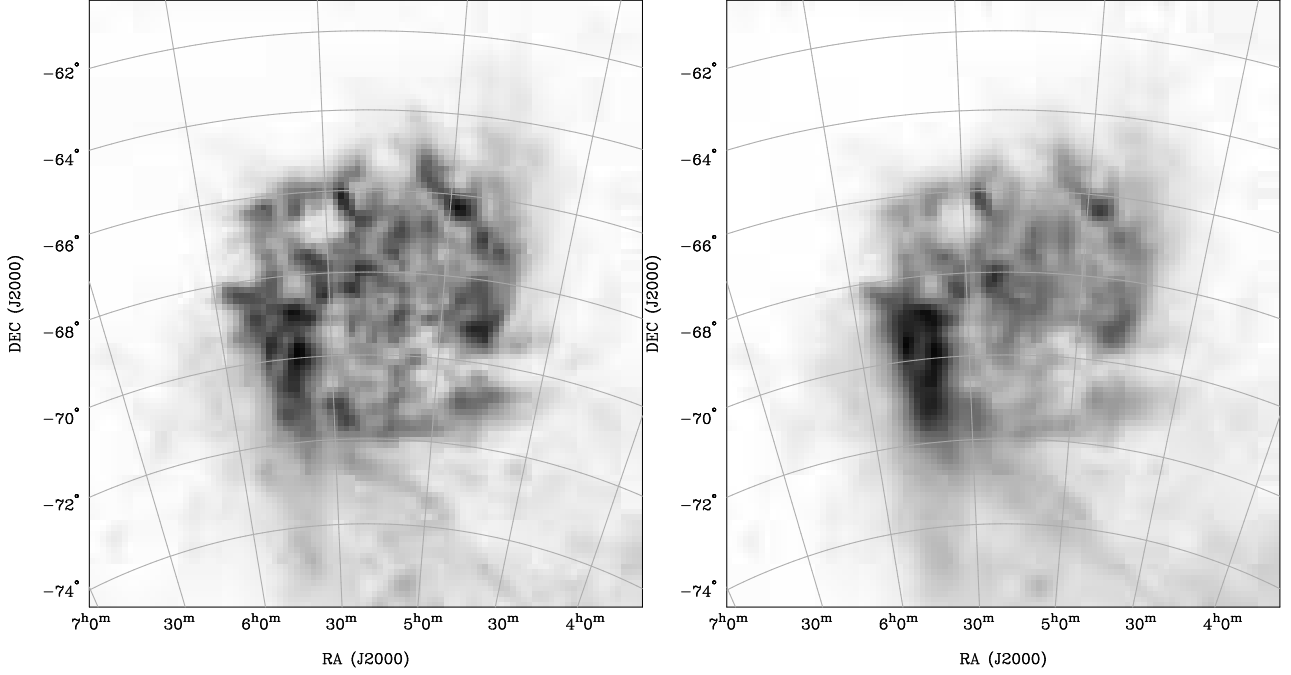


Figure 3. (Left) Peak brightness-temperature image of the LMC showing, for each position, the maximum value of T_B in the heliocentric velocity range 100 to 430 km s⁻¹. The full intensity range 0 to 83.1 K is shown. (Right) Column density image over the same velocity range, formed by summing all emission brighter than 0.08 K (3- σ). The full column density range 0 to 5.6×10^{21} cm⁻² is shown. Both images use a square root transfer function.

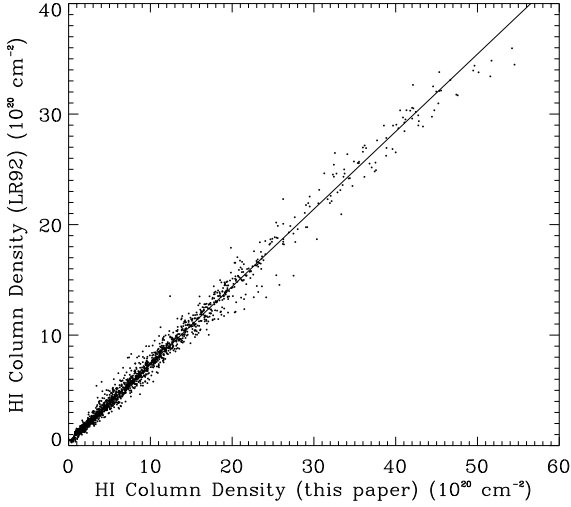


Figure 4. A pixel–pixel comparison of H I column densities from Luks & Rohlfs (1992) with the present data. The slope of the fit (least absolute deviation) is 0.70. For all points, the mean absolute deviation along the y -axis is 4.3×10^{19} cm⁻². For column densities $< 10^{21}$ cm⁻², the mean absolute deviation is 2.9×10^{19} cm⁻². Pixels at the highest column densities fall below the regression line. This may reflect the slightly different angular resolutions of the two surveys.

east-west gap centred at RA 05^h00^m, Dec. $-70^\circ 12'$ (J2000) and bounded by LMC 2 and arm S. This void includes LMC 8, LMC SGS 4 (Meaburn 1980, Kim et al. 1999) but is sub-

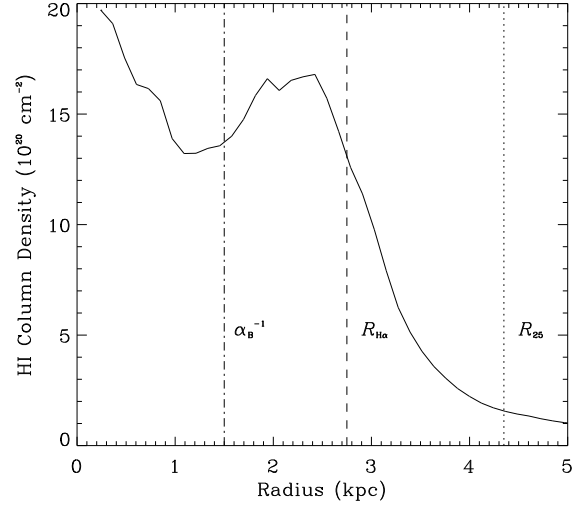


Figure 5. Azimuthally averaged H I column density profile of the LMC in units of 10^{20} cm⁻². The dynamical centre at RA 05^h17^m6, Dec. $-69^\circ 02'$ (J2000) (Kim et al. 1998a) has been used, and a distance to the LMC of 50 kpc has been assumed. The mean column density is highest near the centre of the LMC, and the disk of the LMC appears to be limb-brightened. Various optical disk radii are marked: the B scale length, α_B^{-1} ; the H α radius; and the radius at $\mu_B = 25$ mag arcsec⁻², R_{25} . See Table 1 for details.

stantially larger. This void is discussed in Section 4 and the population of H I holes is further discussed in Section 5.

- The body of the LMC exhibits limb-brightening in

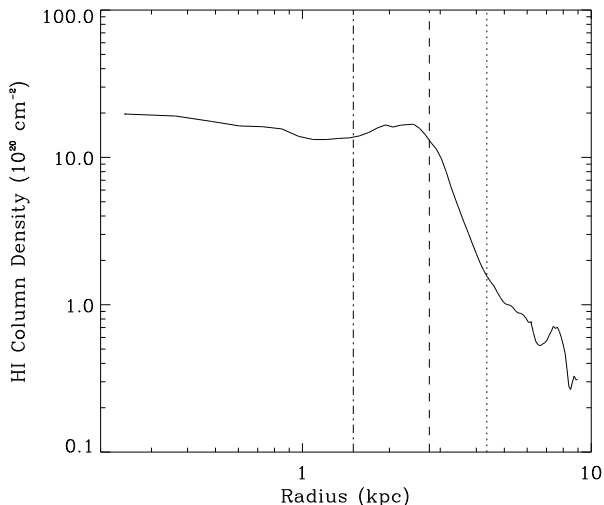


Figure 6. Azimuthally averaged HI column density profile of the LMC in units of 10^{20} cm^{-2} . As Fig. 5, but plotted logarithmically and with an extended range of radii. The vertical lines mark the optical diameters as detailed in Fig. 5.

HI as shown in the surface density profile of Fig. 5. The azimuthally-averaged surface density peaks at $2 \times 10^{20} \text{ cm}^{-2}$ near the dynamical centre, but also again at radius 2.2 kpc where it reaches $1.7 \times 10^{20} \text{ cm}^{-2}$. The limb-brightening is accentuated by arm E and the body of gas near LMC 2 and 30 Doradus in the south-east, especially in the column density image, and by arms S and W in the south and west, respectively. The column density increase in the south-east is sometimes identified as compression arising from the proper motion of the LMC through the tenuous halo of the Milky Way (e.g. de Boer et al. 1998).

- Diffuse gas is present around much of the LMC, especially at pa's from 90° to 330° . At 5 kpc radius, Fig. 5 shows that the mean column density remains $1 \times 10^{20} \text{ cm}^{-2}$. A logarithmic version of the surface density profile is shown in Fig. 6. This shows that, although there is a rapid decrease in column density beyond 2.5 kpc, there is no cutoff. The surface density decrease is approximated by $\Sigma(\text{HI}) \propto r^{-3.3}$. This is shallower than the exponential profile which seems to characterise the late-type dwarf galaxies studied by Swaters (1999).

- The main arms B and E both emanate, at different velocities, from the south-east of the LMC. These arms appear to be associated with much of the diffuse gas in the southern half of Fig. 3. These arms are unlikely to be coplanar (see Section 3.4). Arm S is also clearly visible, and appears to be associated with some of the diffuse gas in the west. Arm W is less visible and more curved in Fig. 3 than in the channel maps and may therefore be a superposition of several components. As has been noted by several authors recently (Kim et al. 1998a; Gardiner et al. 1998) that, although disturbed, the LMC has distinct spiral features. This is in contrast with the near-infrared map of the stellar distribution (van der Marel 2001) which, aside from the bar and bar-related arm-like features, is remarkably uniform.

The main features in the outer body of the LMC are summarised in Fig. 1.

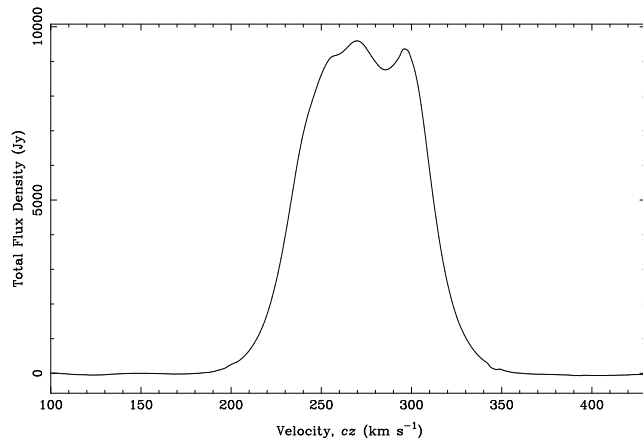


Figure 7. A global HI profile of the LMC. The spectrum has been spatially integrated in a rectangular region of dimensions 9.4×12.7 (RA and Dec., respectively) centred on RA $05^{\text{h}}17^{\text{m}}36^{\text{s}}$, Dec. $-69^\circ02'$ (J2000). Global parameters are summarised in Table 1.

3.3 Spatially Integrated Properties of the LMC

Assuming a distance of 50 kpc and optically thin emission, the column density image in Fig. 3 can be integrated to give a total HI mass for the LMC, $M_{\text{HI}} = (4.8 \pm 0.2) \times 10^8 M_\odot$ (Table 1). McGee & Milton (1966) quote a similar value, $5.0 \times 10^8 M_\odot$ (adjusted to the distance scale used here), though they applied an optical depth correction based on a spin temperature of 200 K. As already noted, LR92 quote a smaller value, $3.1 \times 10^8 M_\odot$. Their survey was limited in spatial extent. When our image is integrated over the same area, the mass remains 30 per cent higher than quoted by LR92. Possible reasons for this have already been given. It is worth mentioning that our new mass estimate makes the LMC HI mass higher than that of the SMC which is $4.2 \times 10^8 M_\odot$ (Stanimirović et al. 1999). The isodensity ($> 10^{20} \text{ cm}^{-2}$) mass and disk mass (radius < 3.5 kpc) of the LMC are also listed in Table 1.

For comparison with other late-type galaxies, the spatially-integrated HI spectrum of the LMC is shown in Fig. 7. The area integrated in this figure is centred on the dynamical centre of Kim et al. (1998a). The heliocentric velocity (mean and V_{50}) is 273 km s^{-1} , similar to the Kim et al. (1998a) kinematic value of 279 km s^{-1} and the LR92 kinematic value of 274 km s^{-1} . We summarise velocity and velocity width parameters in Table 1.

Table 1 shows that the ratio of the HI to total mass in the LMC disk is 8%, the HI mass to blue luminosity ratio is $0.21 M_\odot/L_\odot$, and the star formation timescale ($M_{\text{gas}}/\text{SFR}$) is 2.4 Gyr, where we have assumed a 30% He contribution. The HI mass is a factor of 10 higher than the condensed molecular mass estimated by Fukui et al. (1999), and a factor of 60 higher than the diffuse molecular mass measured by Tumlinson et al. (2002). The HI diameter of the LMC at $1 M_\odot \text{ pc}^{-2}$ is 9.3 kpc and the ratio of the HI diameter to the optical diameter is $D_{\text{HI}}/D_{25} = 1.1$, in line with the mean value for spirals of 1.7 ± 0.5 (Broeils & Rhee 1997), though less than the mean value for late-type dwarf galaxies of 3.3 ± 1.5 (Swaters 1999). As its absolute magnitude of $M_B = -17.9$ mag and its morphology indicate, the LMC

Table 1. Global properties for the LMC based on distance of 50 kpc.

Parameter	Units	Value	Reference
Total H I mass, M_{HI}	M_{\odot}	4.8×10^8	This paper
Isodensity mass ($> 10^{20} \text{ cm}^{-2}$)	M_{\odot}	4.6×10^8	This paper
Disk H I mass ($< 3.5 \text{ kpc}$)	M_{\odot}	3.8×10^8	This paper
H I diameter (10^{20} cm^{-2})	kpc	10.2	This paper
H I diameter, D_{HI} ($1 M_{\odot} \text{ pc}^{-2}$)	kpc	9.3	This paper
Heliocentric velocity, V_{50}	km s^{-1}	273	This paper
Velocity width, W_{50}	km s^{-1}	80	This paper
Velocity width, W_{20}	km s^{-1}	102	This paper
Foreground extinction, $< E_{B-V} >$	mag	0.06	This paper
Total dynamical mass ($< 4 \text{ kpc}$), M_T	M_{\odot}	5×10^9	Kim et al. (1998a), Alves & Nelson (2000)
Molecular mass	M_{\odot}	$(4 - 7) \times 10^7$	Fukui et al. (1999)
Blue luminosity ^a , L_B	L_{\odot}	2.3×10^9	de Vaucouleurs et al. (1991)
Blue diameter, D_{25}	kpc	8.7	Bothun & Thompson (1988), de Vaucouleurs et al. (1991)
Blue scale length, α_B^{-1}	kpc	1.5	Bothun & Thompson (1988)
H α luminosity	erg s^{-1}	2.7×10^{40}	Kennicutt et al. (1995)
H α diameter	kpc	5.5	Kim et al. (1999)
Star Formation Rate, SFR	$M_{\odot} \text{ yr}^{-1}$	0.26	Kennicutt et al. (1995)
M_{HI}/M_T ($< 4 \text{ kpc}$)		0.08	
M_{HI}/L_B	M_{\odot}/L_{\odot}	0.21	
$(M_{\text{HI}} + M_{\text{He}})/\text{SFR}$	yr	2.4×10^9	
D_{HI}/D_{25}		1.1	
$D_{\text{HI}}/\alpha_B^{-1}$		6.2	

^a Based on $B_T^{\circ} = 0.57$ (de Vaucouleurs et al. 1991) and $M_B(\odot) = 5.50 \text{ mag}$ (Lang 1991).

has properties somewhat closer to those of spiral galaxies than to those of late-type dwarf galaxies.

3.4 Tidal and other Interaction Features

In Section 3.1, we referred to arms B, E and W which are marked in Fig. 1. Arm B leads directly into the Magellanic Bridge where it appears to merge with SMC gas, possibly explaining the multiple-peaked emission profiles in this region (McGee & Newton 1986). The Bridge appears to be tidal in origin and, in the model of Gardiner & Noguchi (1996), was formed 0.2 Gyr ago. The existence of arm B demonstrates the presence of some LMC gas in the Bridge, although the major component is undoubtedly stripped from the lower-mass SMC. Arm B consists of at least two separate filaments with a separation of up to $\sim 0.5^{\circ}$ (see Figs 1 & 3). The velocity differential between the filaments was sufficient to warrant listing the position RA $04^{\text{h}}58^{\text{m}}36^{\text{s}}$, Dec. $-73^{\circ}33'57''$ (J2000) as the centre of the candidate supergiant shell LMC SGS 1 by Kim et al. (1999).

Arms E and W lead directly south and north, respectively, of their starting point in the LMC. As already noted, arm E points to the beginning of the Leading Arm clouds mapped by Putman et al. (1998). Although these clouds lie 4° beyond the edge of the present map, deep reprocessed HIPASS data (Putman et al. 2002) show a continuous connection between this point and the Leading Arm at heliocentric velocities between 260 and 300 km s^{-1} . Arm W leads directly north, extending into the diffuse gas to the north-west at $\sim 270 \text{ km s}^{-1}$. As noted by Putman et al. (2002) and seen in their Fig.5, this gas then seems to bypass the

Bridge and makes what appears to be a direct connection with the Magellanic Stream..

What causes the arm-like features arms E and W? As with spectacular systems such as NGC 4038/4039 (the ‘‘Antennae’’; Hibbard et al. 2001), a plausible explanation is again tidal interaction. But in this case, the tidal force arises from the Galaxy and not the SMC. As Fig. 1 shows, the great circle to the Galactic Centre lies directly south[†] of the LMC, therefore the tidal force projects along this line, at more or less the same position angle as the two arms. The two arms E and W may be wound up due to the LMC’s clockwise rotation (Kroupa & Bastian 1997).

It is unusual that arms B and E appear to emanate from similar points at the south-east of the LMC, with the former flowing into the Bridge and the latter flowing into the Leading Arm. The chronology of events is likely to be that the gaseous tide in the LMC was disturbed by the SMC’s close passage 0.2 Gyr ago, funnelling a portion of the gas near the LMC-Galaxy Lagrangian L1 point into the Bridge. At the present time, the tidal force ($\propto M/R^3$) from the Galaxy is likely to be many times stronger than that from the SMC. For an LMC total mass of $5 \times 10^9 M_{\odot}$ (Kim et al. 1998, Alves & Nelson 2000) a distance of 50 kpc, an SMC total mass of $1.5 \times 10^9 M_{\odot}$ and an SMC/LMC separation of 22 kpc (Staveley-Smith et al. 1998), the tidal force ratio[§]

[†] For an LMC/Galaxy mass ratio of 0.01, the LMC-Galaxy Lagrangian L1 point only lies $\sim 5 \text{ kpc}$ in front of the LMC (and because of parallax, $\sim 1^{\circ}$ south).

[§] As an aside, the predicted tidal force of the Galaxy on the

is ~ 30 . However, for an encounter at 7 kpc the force ratio would be unity.

Current numerical models predict that most of the gas in the Leading Arm (and the Stream) comes from the SMC, (Gardiner & Noguchi 1996; Li 1999), with the LMC merely serving to disrupt the Leading Arm which passes in front of it. However, it seems to be the case that, as with the Bridge, significant LMC gas is ‘leaking’ into the Leading Arm. Metallicity measurements of Leading Arm clouds such as HVC 287.5+22.5+240 (Lu et al. 1998) may give clues as to the ratio of LMC gas to the slightly less-enriched SMC gas.

Cepheid distances (Welch et al. 1987) suggest that the closest part of the LMC is at $pa\ 77^\circ \pm 42^\circ$. Recent AGB and RGB stellar distances give a more accurate near-side pa of $32^\circ \pm 8^\circ$ (van der Marel & Cioni 2001). Therefore, the north-eastern part of the disk is the closest to the Galaxy, closest to the L1 point and the most easily perturbed by the SMC. This is not inconsistent with the point of origin of arms B and E.

A suggested geometry for the LMC tidal features is that arms B and E both arise from the outer parts of the LMC in the east. The arms extend southwards where they bifurcate at a position close to the LMC tidal radius. The low-velocity arm B swings around, probably upwards out of the plane of the LMC, curves around to the south-west where it eventually joins the Magellanic Bridge at somewhat larger distances than the LMC. This feature is evident in the simulations of Li (1999). The high-velocity arm E extends directly south, probably remaining at the same Galactocentric distance as the LMC. It then joins the general Leading Arm gas which mainly arises from the SMC. The large amount of star-formation in the 30 Doradus region may well be a manifestation of the tidal shear occurring in the region near the origin of arms B and E.

However, the question remains as to why the near-infrared stellar distribution is so smooth in the outer parts of the LMC. van der Marel (2001) reports no clearly discernable spiral structure at radii out to 9° , which is beyond the radius surveyed in this paper. Tidal distortion must apply to stars as well as gas, and the usual argument that the HI is well outside the stellar distribution does not apply. Could it be that the evolved stars in the 2MASS and DENIS images are not tracing the same thin disk as the HI? Or has orbit-crossing and dissipation made the HI density evolve in a non-linear manner? The significant gas self gravity ($\sim 10\%$ of the total mass is in the form of HI and He; see Table 1) makes the latter a distinct possibility. Nevertheless, the stellar distribution shows strong evidence of tides. van der Marel (2001) argues that the distribution of stars is significantly elongated in the direction of the Galactic Centre, as predicted by tidal theory.

The diffuse gas in Fig 3, and labelled in Fig. 1 appears to

be strongly related to the tidal arms. The gas in the south-east occurs at similar velocities to arm E. In the channel maps (Fig.2), some of this gas at 290 km s^{-1} itself falls into diffuse linear features. The more extensive HIPASS data again shows a connection to the Leading Arm. This would tend to argue for a tidal origin for this gas also. Weinberg (2000) also points out the dramatic effect of the Galaxy on the LMC’s stellar structure through torquing of disk orbits and tidal stripping, and suggests a mass-loss rate of $3 \times 10^8\text{ M}_\odot$ per orbit, even without the SMC. He also predicts tidally stripped stars some tens of kiloparsecs away from the LMC, which have possibly already been seen in the 2MASS data (Weinberg & Nikolaev 2001). With an LMC inclination of $\sim 30^\circ$, and a line-of-nodes at $pa \sim 0^\circ$, the spin vectors of the Galaxy and the LMC are perpendicular, a geometry not suitable for strong tidal interaction. However, if the higher values for the inclination and pa suggested by van der Marel (2001) are correct, then the spin vectors of the Galaxy and the LMC will be better aligned, and the current interaction will be stronger.

For the diffuse gas in the south-east, it is also worth noting that ram pressure is a viable alternative. Any gas outside the influence of the LMC which is slowed by ram pressure will tend to drop in its orbit around the Galaxy. By doing this, its angular velocity increases and it will tend to lead the LMC, unless dynamical friction on the LMC is more important (Moore & Davis 1994). Although Murali (2000) suggests that ram pressure is not a viable possibility for a remnant as old as the Magellanic Stream (otherwise there is too much evaporation), this argument does not apply to the clouds near the LMC. On the other side of the LMC, the diffuse gas to the south-west is clearly associated with the Bridge.

As well as having a strong tidal influence on the LMC and SMC, the Galaxy has left a clear tidal signature on the Sagittarius dwarf galaxy which is responsible for a trail of stars forming a great circle on the sky (Ibata et al. 2001). Martínez-Delgado et al. (2001) confirm the existence of tidal tails in Ursa Minor, a dwarf spheroidal galaxy lying at a distance of 70 kpc. Other objects such as the Carina dwarf spheroidal galaxy also appear to have stellar distributions which are radially truncated (Majewski et al. 2000). However, a lack of a clear understanding of the internal dynamical state of these systems has contributed to an uncertainty about whether the truncation can strictly be interpreted as tidal in origin.

The importance of tidal signatures in satellite galaxies lies in their usefulness in measuring the total mass of the Milky Way, the extent of its dark halo, and for detecting any sub-structure within the halo. Present results for the LMC and the Magellanic Stream appear to confirm the existence of a massive halo around the Galaxy, with the total mass out to a radius of 50 kpc of $\sim 5 \times 10^{11}\text{ M}_\odot$. However, the existence of tidal debris around the LMC complicates interpretation of results from the MACHO experiment (Alcock et al. 2000) which attempted to measure the fraction of the Galaxy’s dark halo in the form of compact objects. Stars which are tidally stripped and lie slightly behind the LMC, rather than in a thin disk, substantially contribute to the frequency of microlensing events (Weinberg 2000). This implies that the measurement of the Galactic halo mass in the form of compact objects (currently $\sim 10^{11}\text{ M}_\odot$) should

LMC in Milgrom’s (1983) theory of modified Newtonian dynamics (MOND) is more or less the same as the Newtonian prediction. However, because there is little requirement for dark matter in the SMC even in the Newtonian model, the tidal force in the MOND regime ($\propto M/R^2$) will be relatively stronger. Thus the Magellanic system, and similar multiple systems may be useful laboratories for studying inertia and gravity at low accelerations).

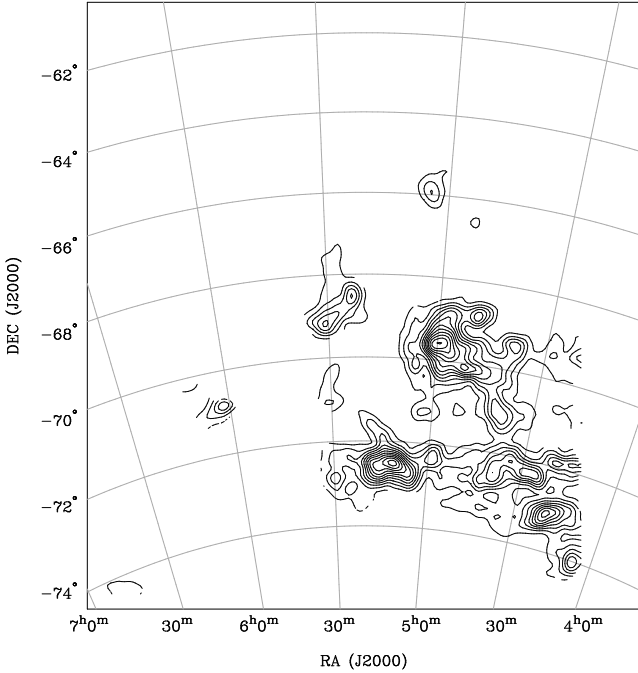


Figure 8. H I column density contours of high-velocity clouds. The heliocentric velocity range 115 to 176 km s^{-1} is included. Contours are in steps of $2 \times 10^{18} \text{ cm}^{-2}$ starting at $2 \times 10^{18} \text{ cm}^{-2}$. Noisy regions at the edge of the image have been excluded. The map has been smoothed by a Gaussian of FWHM $12'$, and was derived by applying a smooth mask to the data cube in order to isolate those regions with significant column density. Many of the high-velocity clouds shown here are probably connected to the LMC. The peak column density of $2.4 \times 10^{19} \text{ cm}^{-2}$ occurs at $04^{\text{h}}59.3^{\text{m}}$, Dec. $-69^{\circ}35'$ (J2000) which is the position of an H I void and the supergiant shells LMC 8 and LMC SGS 4 (which are also discussed in Section 5).

probably be regarded as an upper limit until the geometry of the halo of the LMC is better understood.

4 THE HALO OF THE LMC

Because the present study has velocity information, we can attempt to probe the LMC's halo by searching for H I at anomalous velocities. Such gas is expected to occur due to outflows from star-forming regions and stripping of the outer disk due to tidal and ram pressure forces. Non-planar occurrence of gas and stars has previously been reported or suggested by Luks & Rohlfs (1992), Zaritsky & Lin (1997), Wakker et al. (1998) and Graff et al. (2000) and, as reported by the latter, is an important factor in determining the self-lensing optical depth of the LMC. Of particular interest are the HVC complexes below $+180 \text{ km s}^{-1}$, whether they belong to the Galaxy or the LMC. de Boer, Morras & Bajaja (1990) use an H I strip scan to conclude that the gas at LSR velocities $+70$ and $+140 \text{ km s}^{-1}$ is Galactic in origin. Richter et al. (1999) concur, suggesting that the $+120 \text{ km s}^{-1}$ H₂ absorption feature seen against HD269546 is an HVC originating in the disk of our Galaxy.

Fig. 8 shows the prominent HVCs (column densities over $2 \times 10^{18} \text{ cm}^{-2}$) with velocities in the range 115 to 176 km s^{-1} (heliocentric). They are extensive over much

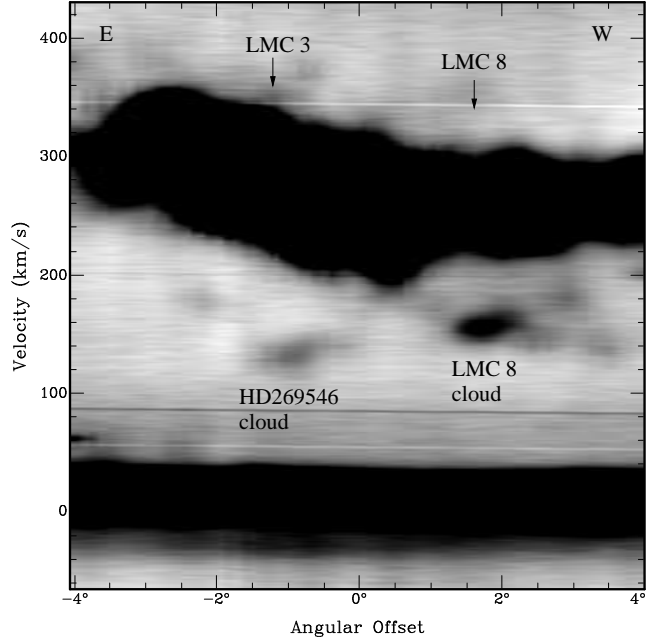


Figure 9. An H I position-velocity slice centred on $05^{\text{h}}17^{\text{m}}02^{\text{s}}$, Dec. $-68^{\circ}49'19''$ (J2000) at pa 250° . The emission from the LMC (at $\sim 260 \text{ km s}^{-1}$) and the Galaxy (at $\sim 10 \text{ km s}^{-1}$) has been saturated to reveal the faint emission from the HD269546 absorbing cloud (Richter et al. 1999) at $05^{\text{h}}27^{\text{m}}$, Dec. $-68^{\circ}50'$ (J2000), 131 km s^{-1} (heliocentric) and the LMC 8 cloud at $04^{\text{h}}59^{\text{m}}$, Dec. $-69^{\circ}35'$ (J2000), 155 km s^{-1} (heliocentric). The data has been smoothed with a Gaussian FWHM of $20'$. The narrow feature at $\sim 85 \text{ km s}^{-1}$ is an artefact.

of the south-west LMC, but extend elsewhere in the field at lower column densities. Some or most of the emission in the south-west lies projected between arms B and S, and is likely related to the Bridge and the tidal interaction with the SMC. However, the peak column of $2.4 \times 10^{19} \text{ cm}^{-2}$ projects onto the position of the giant H I void containing LMC 8 (Meaburn 1980) and LMC SGS 4 (Kim et al. 1999) (see also Sections 3.2 and 5). Oey et al. (2002) show a high-resolution H I mosaic of this region which also contains the superbubbles DEM L25 and L50. Moreover, the HD269546 absorbing cloud seen by Richter et al. (1999), which has a peak column density $1.0 \times 10^{19} \text{ cm}^{-2}$, is at RA $05^{\text{h}}27^{\text{m}}$, Dec. $-68^{\circ}50'$ (J2000) which corresponds to the H I void at LMC 3 (Meaburn 1980) and LMC SGS 12 (Kim et al. 1999). This suggests that this gas has been removed from the LMC disk. A position-velocity cut across both the HD 269546/LMC 3 and the LMC 8 clouds is shown in Fig. 9. The latter shows clear connections with LMC gas. The former shows a probable connection at low column density. At other pa's, both complexes also appear to have gas at velocities higher than the LMC disk. This suggests an explosive origin for the gas, rather than a tidal or ram-pressure-stripped origin. However, the kinematics of the high-velocity gas are not simple, and certainly cannot be modelled as a simple expanding bubble, or double-sided mushroom cloud.

The association of some high-velocity clouds with the LMC implies that the outflow velocities, however they are attained, are substantial. In the case of the HD269546 cloud, the mean velocity differs by 126 km s^{-1} from systemic. In the case of the LMC 8 cloud, the mean velocity differs by 97

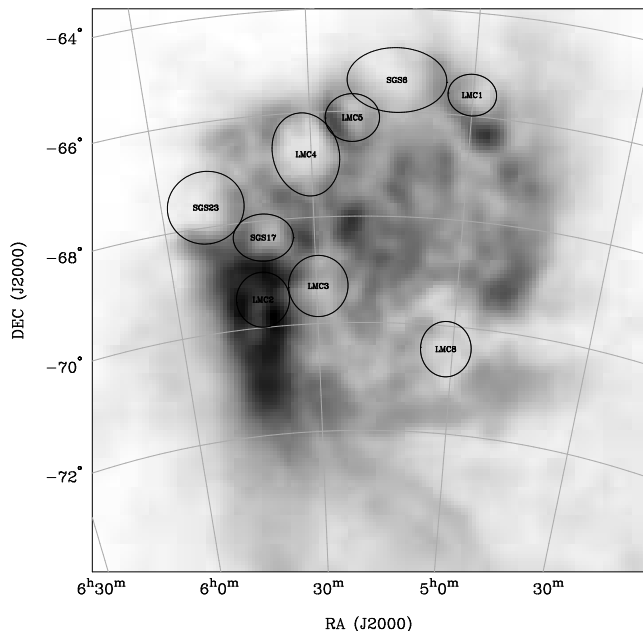


Figure 10. Supergiant shells from Meaburn (1980) (LMC 1 – 5 and 8) and Kim et al. (1999) (LMC SGS 6, 17 and 23) are overlaid on the H I column density image (slightly enlarged compared with Fig. 3) if they coincide with clear H I holes at the resolution of the Parkes data. The shells LMC 1 to 5 and 8 are also known as LMC SGS 3, 19, 12, 11, 7 and 4, respectively.

km s⁻¹ from systemic. Outflows at these velocities ought to be accompanied by X-ray as well as the H α emission already known to be present. However, the strength depends on the density of the medium being shocked. Because a substantial H I column is present in the HD269546 cloud, its temperature is lower than 10⁴ K, but higher than the lower limit to the H₂ excitation temperature of 10³ K measured by Bluhm et al. (2001). These clouds probably exist in a cocoon of hotter material. Bluhm et al. (2001) suggest a neutral hydrogen fraction of 5–20%, from observations of O and O⁺.

The height of the neutral clouds above the LMC disk can only be speculated. The projected radii of LMC SGS 4 and 12 (Kim et al. 1999) provides a weak lower limit of ~ 0.5 kpc. The $\sim 30^\circ$ inclination of the LMC possibly provides an upper limit of a few kpc, otherwise the non-planar gas would project elsewhere on the LMC disk (though this may indeed be the case for much of the gas in Fig. 8).

5 H I HOLES

Several holes, or gaps in the H I column density image in Fig. 3 are apparent. As originally noted by Westerlund & Mathewson (1966), the positions of some holes show a very strong correlation with stellar associations, H II regions and SNRs. Six of the nine candidate supergiant H α shells listed by Meaburn (1980) are clearly associated with holes. These shells are marked in Fig. 10. LMC 1, 4 and 5 are well-aligned with an H I hole; LMC 2 and 3 are more complex than simple circular holes; and LMC 8 is associated with an H I hole that is at least twice as large as the H α shell. In addition to the six Meaburn shells shown in Fig. 10, Kim et al. (1999) list a further 17 supergiant shells. Some of the largest of these

(LMC SGS 6, 17 and 23) are also clearly visible as H I holes in Fig. 10.

As discussed by Kim et al. (1999), there is a good association between H I and H II regions, and some evidence for regions of star-formation providing direct mechanical input into the expansion of the shells and therefore the evacuation of the H I. However, Wada et al. (2000) point out that thermal and gravitational instabilities can also lead to the formation of cavities and filaments. In cases like LMC 4, numerous studies (Dopita et al. 1985, Domgörgen et al. 1995, Efremov & Elmegreen 1998, Olsen et al. 2001) paint a picture of progressive star-formation propagating outwards from the centre of the shell. Ionization, dynamical pressure and conversion to molecules and stars depletes the H I, with the remainder forming a rim where the newest star-formation occurs. In other cases such as LMC 2, the geometry is more complex and, although energy input by stellar winds and supernovae (Weaver et al. 1977) may dominate, the simple model of outwardly propagating star-formation requires modification (Points et al. 1999, 2000). Finally, in cases such as LMC SGS 6 (Kim et al. 1999), no correlation between H I and anything else is evident. In these cases, it is possible that an older population of stars whose initial mass function was skewed towards higher mass stars is responsible. However, it is also possible that other dynamical events are responsible.

For each of the holes marked in Fig. 10, we have plotted a position-velocity slice in Fig. 11. These slices commonly show a dip in the column density at the position of the hole (except where the image is saturated), evidence for a velocity gradient which reflects the rotation of the LMC, and, in some cases, evidence for high-velocity gas. LMC 2, 4 and LMC SGS 17 and 23 show evidence for multiple velocity components close to the systemic velocity ($\Delta V \sim 20$ km s⁻¹) and which may be construed as continued slow momentum or pressure-driven expansion of gas away from the interior of the evacuated shell. In addition, most of the holes (except LMC 4 and LMC SGS 6) show evidence for higher velocity gas ($\Delta V \sim 100$ km s⁻¹) at low column densities (as discussed in Section 4 for LMC 3 and 8). The origin of this gas and its definite association with the H I holes remains unclear. However, expulsion by stellar and supernova shocks, or other explosive events, remains a good possibility. Further studies of the coronal gas towards such regions (e.g. Bomans et al. 1996, Wakker et al. 1998) are desirable.

6 THE GALACTIC FOREGROUND

Its closeness, favourable inclination and low internal extinction make the LMC an ideal object to study in the optical for many purposes. However, its mean Galactic latitude of -34° means that foreground extinction is of some importance. *IRAS* is unable to separate LMC dust from Galactic dust (although Schwering & Israel 1991 attempted to incorporate low resolution H I data to isolate the foreground component). For example, the LMC, SMC and M31 are not removed from the *IRAS*/DIRBE extinction maps of Schlegel, Finkbeiner & Davis (1998). Around the outskirts of the LMC, the maps of Schlegel et al. (1998) show a variation from $E_{B-V} = 0.04$ to the north-west of the LMC to around 0.12 in the south-west, implying that extinction is significant, and variable. The SMC, lying slightly further from the Galactic Plane ap-

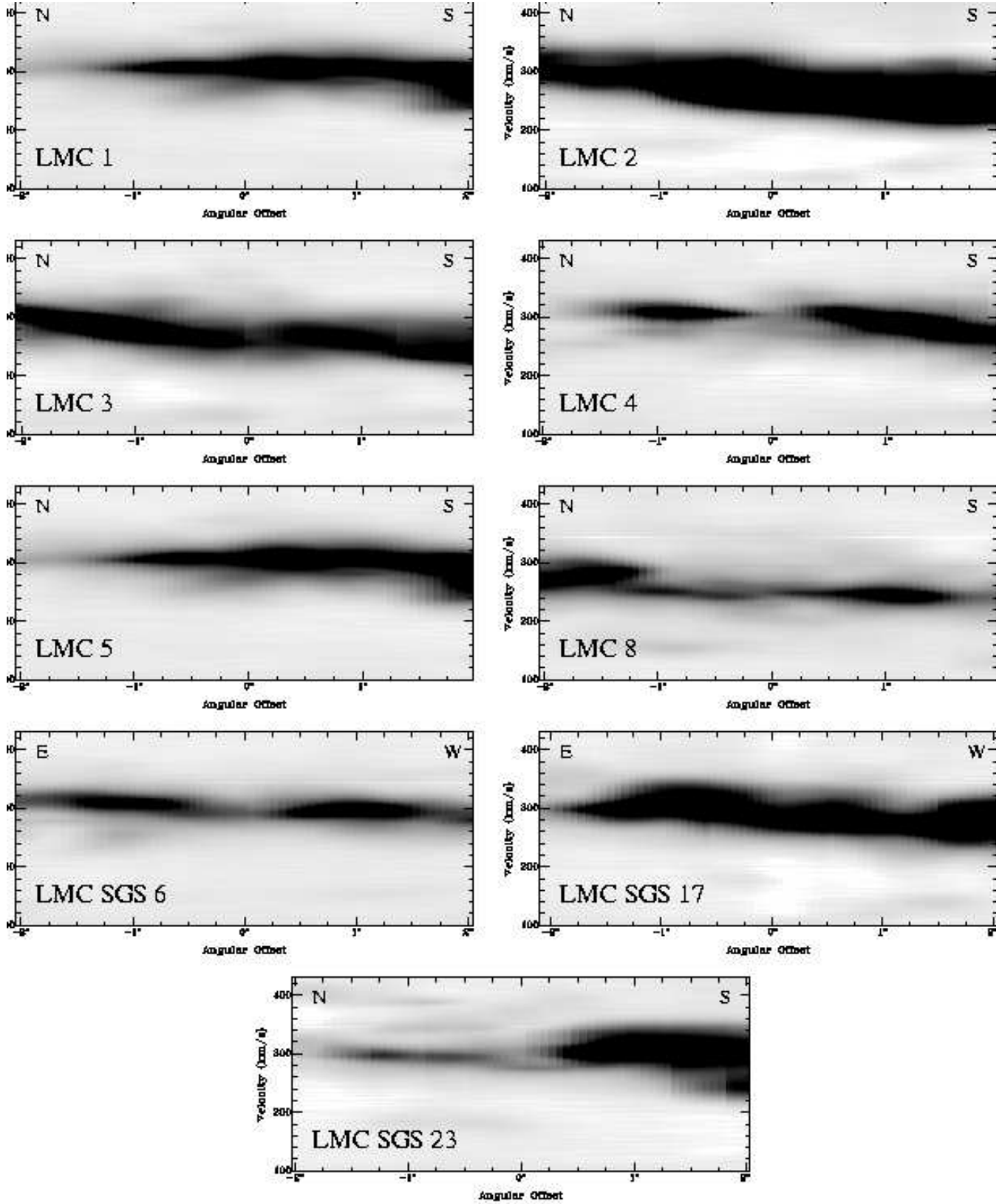


Figure 11. Position-velocity slices across the H I holes marked in Fig. 10. The slices are generally at pa 0° except for LMC 4 (10°), LMC SGS 6 (90°) and LMC SGS 17 (85°). To bring out fainter features, the greyscale is saturated at 9 K. High-velocity gas appears to be associated with some of the holes (e.g. LMC 4), but in only two cases (LMC SGS 17 and 23) is there some evidence for a complete shell. The data have been smoothed with a Gaussian FWHM of 20'.

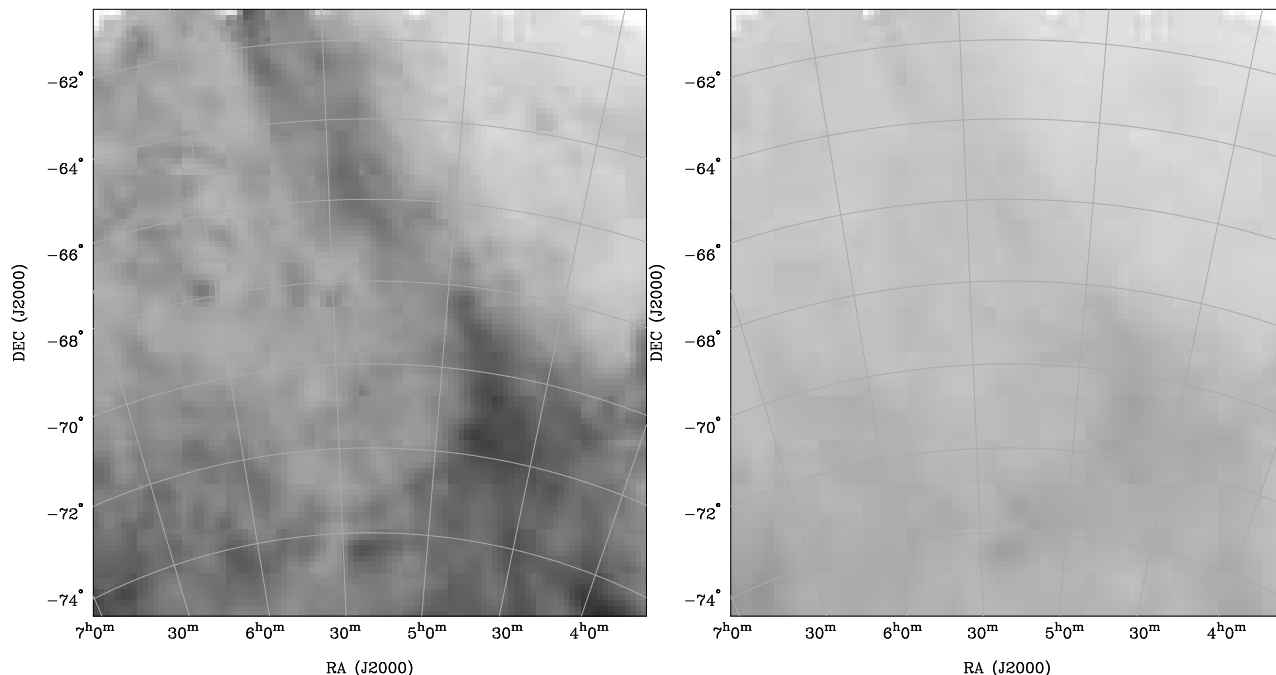


Figure 12. (Left) Peak brightness-temperature image of the Galactic gas in the foreground of the LMC showing, for each position, the maximum value of T_B in the heliocentric velocity range -64 to 100 km s^{-1} . The intensity range and transfer function is the same as for Fig. 3, although the peak temperature for the Galactic gas is lower, 56.3 K . (Right) Column density image over the same velocity range, formed by summing all emission brighter than 0.08 K (3σ). The column density range is the same as for Fig. 3, with the maximum column density for the Galactic gas being $1.3 \times 10^{21} \text{ cm}^{-2}$.

appears to lie in a region with foreground extinction at the lower end of this range. A strong linear feature, now known to be associated with Galactic gas and dust also complicates the picture (de Vaucouleurs 1955, McGee et al. 1986).

Because there appears to be no Galactic gas $> 100 \text{ km s}^{-1}$, or LMC gas $< 100 \text{ km s}^{-1}$, there is a clean separation of the Galactic and LMC components in the H I data. Fig. 12 shows the peak brightness-temperature and column density images for the Galactic component using the same intensity range as the LMC images in Fig. 3. The Galactic component is smoother with a maximum column density around a quarter of that in the LMC, and a maximum temperature of around two-thirds of the LMC value. There is a significant column-density gradient from north-west to south-east and a significant filament extending from the north at RA $05^{\text{h}}38^{\text{m}}$, Dec. $-62^{\circ}26'$ (J2000) to RA $04^{\text{h}}39^{\text{m}}$, Dec. $-70^{\circ}50'$ (J2000) in the south-east. Contours of H I column density are shown in Fig. 13 along with E_{B-V} contours based, for reference, on equation (7) of Burstein & Heiles (1978).

Over the disk of the LMC, the mean Galactic extinction is $< E_{B-V} > = 0.06 \text{ mag}$ with a range between 0.01 and 0.14, and an rms of 0.02 mag. The extinction gradient is from north-west to south-east, with a systematic variation of $\Delta E_{B-V} \approx 0.1 \text{ mag}$ over the full field. Although significant in B ($\Delta A_B \approx 0.4 \text{ mag}$), the variation in H is small ($\Delta A_H \approx 0.06 \text{ mag}$) and should only affect the details of infrared structural results (Weinberg & Nikolaev 2001, van der Marel & Cioni 2001) rather than modify their overall conclusions. As pointed out by Schwing & Israel (1991), 30 Doradus has a low foreground extinction ($E_{B-V} = 0.05$). The LMC values agree with: the mean of $0.06 \pm 0.02 \text{ mag}$

and range of 0.00 to 0.15 mag from the cool star data of Oestreich, Gochermann & Schmidt-Kaler (1995) (see also Zaritsky 1999); a mean of 0.06 mag from a combination of polarisation and H I data by Bessell (1991); and the range 0.07 to 0.17 mag suggested by Schwing & Israel (1991) from a combination of H I and *IRAS* data.

Finally, it should be emphasised that the H I data alone has zero-point problems due to a combination of spillover radiation and intrinsic variations in gas-to-dust ratio. However, the range of *IRAS*/DIRBE extinctions around the LMC (0.04 to 0.12) is similar to the range, derived from the present H I data (0.01 to 0.14), implying no large systematic problem (the random errors are negligible). Both results are consistent with the combined Galactic and LMC extinctions, measured by Dutra et al. (2001) using background galaxies, of $E_{B-V} = 0.12 \pm 0.10$.

7 SUMMARY

Parkes multibeam observations have been made of neutral hydrogen in and around the Large Magellanic Cloud. The major results are:

- The LMC has a total H I mass of $(4.8 \pm 0.2) \times 10^8 M_{\odot}$ (for an assumed distance of 50 kpc), of which $3.8 \times 10^8 M_{\odot}$ lies within a well-defined disk. This is 8% of the total mass and is a factor of 10 more than the molecular mass so far identified.
- We measure H I column densities which are 43% higher than the previous survey by Luks & Rohlfs (1992).
- Outer tidal arms are identified. These arms appear to

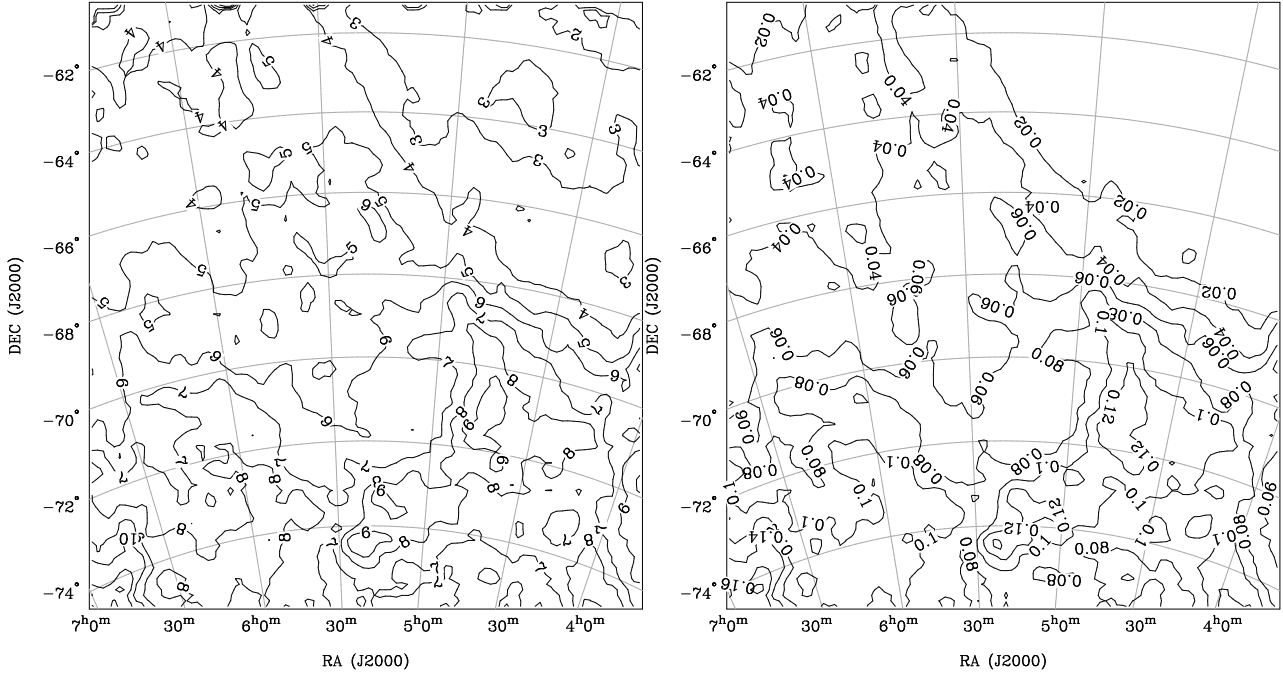


Figure 13. (Left) Contours of H I column density of Galactic foreground gas at heliocentric velocities $< 100 \text{ km s}^{-1}$. Contours are labelled in units of 10^{20} cm^{-2} ; (Right) contours of estimated extinction E_{B-V} due to Galactic foreground dust. Contours are labelled in units of mag.

channel gas into: (a) the Magellanic Bridge, (b) the Magellanic Stream, and (c) the Leading Arm, and appear to be a result of the two-way interaction of the LMC with both the Galaxy and the Small Magellanic Cloud. The gas at $r > 4^\circ$ does not follow the outer stellar contours, suggesting that shocks, self-gravity or, possibly, external ram pressure contribute to their appearance. The existence of tidal shearing in the LMC argues for the presence of a massive Galactic halo, and as emphasised by Weinberg (2000), suggests that care needs to be taken to eliminate self-lensing when LMC gravitational microlensing events are used to measure the density of compact objects in the Galaxy's halo.

- High-velocity clouds, previously seen in absorption against LMC stars appear mainly to belong to the LMC in cases where their heliocentric velocity exceeds about 100 km s^{-1} , and not to the Galactic disk or halo.

- Some of the high-velocity clouds appear to be coincident with H I voids (e.g. LMC 3 and 8), suggestive that these voids were created by explosive events. However, most of the H I voids are just that – they show no clearly defined shells of expanding gas. Presumably, if created by supernova and stellar winds, the giant voids accessible for study at the resolution of the Parkes telescope (i.e. $> 0.7 \text{ kpc}$) have already expanded well outside of the thickness of the LMC disk.

- The Galactic foreground H I emission has been used to provide an image, at 16.4 resolution, of the likely foreground dust extinction over the field of the LMC. The mean Galactic extinction is $< E_{B-V} > = 0.06 \text{ mag}$ within the disk of the LMC. Over the full field imaged, there is an extinction gradient from north-west to south-east of $\Delta E_{B-V} \approx 0.1 \text{ mag}$, corresponding to $\Delta A_B \approx 0.4 \text{ mag}$ and $\Delta A_H \approx 0.06 \text{ mag}$.

ACKNOWLEDGMENTS

We thank Christian Brüns and Agris Kalnajs for helpful discussions, the staff at the Parkes telescope for assistance during the commissioning of the narrow-band system, and Warwick Wilson and the AT electronics group for making the hardware and software work efficiently.

REFERENCES

- Alcock C., et al., 2000, *ApJ*, 542, 281
- Alves D. R., Nelson C. A., 2000, *ApJ*, 542, 789
- Barnes D.G. et al., 2001, *MNRAS*, 322, 486
- Bessell M. S., 1991, *A&A*, 242, L17
- Blondiau M. J., Kerp J., Mebold U., Klein U., 1997, *A&A*, 323, 585
- Bluhm H., de Boer K. S., Marggraf O., Richter P., 2001, *A&A*, 367, 299
- Bomans D. J., de Boer K. S., Koornneef J., Grebel E. K., 1996, *A&A*, 313, 101
- Bothun G. D., Thompson I. B., 1988, *AJ*, 96, 877
- Braun M., 1996, *Astron. Nachr.*, 317, 369
- Broeils A. H., Rhee M.-H., 1997, *A&A*, 324, 877
- Burstein D., Heiles C., 1978, *ApJ*, 225, 40
- de Boer K. S., Braun J. M., Vallenari A., Mebold U., 1998, *A&A*, 329, 49
- Davies R. D., Staveley-Smith L., Murray J. D., 1989, *MNRAS*, 236, 171
- de Boer K. S., Morras R., Bajaja E., 1990, *A&A*, 233, 523
- de Vaucouleurs G., 1955, *AJ*, 60, 126
- de Vaucouleurs G., de Vaucouleurs A., Corwin J. R., Buta, R. J., Paturel G., Fouqué P., 1991, *Third Reference Catalogue of Bright Galaxies*. Springer-Verlag, New York
- Domgörgen H., Bomans D. J., de Boer K. S., 1995, *A&A*, 296, 523
- Dopita M. A., Mathewson D. S., Ford V. L., 1985, *ApJ*, 297, 599

- Dutra C. M., Bica E., Clariá J. J., Piatti A. E., Ahumada A. V., 2001, *A&A*, 371, 895
- Efremov Y. N., Ehlerová S., Palouš J., 1999, *A&A*, 350, 457
- Efremov Y. N., Elmegreen B. G., 1998, *MNRAS*, 299, 643
- Elmegreen B. G., Kim S., Staveley-Smith L., 2001, *ApJ*, 548, 749
- Feast M., 1999, *PASP*, 111, 775
- Fukui Y. et al., 1999, *PASJ*, 51, 745
- Gardiner L. T., Noguchi M., 1996, *MNRAS*, 278, 191
- Gardiner L. T., Turfus C., Putman M. E., 1998, *ApJ*, 507, 35
- Gibson B. K., 1999, *astro-ph/9910574*
- Graff D. S., Gould A. P., Suntzeff N. B., Schommer R. A., Hardy E., 2000, *ApJ*, 540, 211
- Hibbard J. E., van der Hulst J. M., Barnes J. E., Rich R. M., 2001, *AJ*, 122, 2969
- Ibata R., Lewis G. F., Irwin M., Totten E., Quinn T., 2001, *ApJ*, 551, 294
- Johansson L. E. B., Olofsson H., Hjalmarsen A., Gredel R., Black J. H., 1994, *A&A*, 291, 89
- Johnson J. A., Bolte M., Stetson P. B., Hesser J. E., Somerville R. S., 1999, *ApJ*, 527, 199
- Kennicutt R. C., Bresolin F., Bomans D. J., Bothun G. D., Thompson I. B., 1995, *AJ*, 109, 594
- Kim S., Staveley-Smith L., Dopita M. A., Freeman K. C., Sault R. J., Kesteven M. J., McConnell D., 1998a, *ApJ*, 503, 674
- Kim S., Chu Y.-H., Staveley-Smith L., Smith R. C., 1998b, *ApJ*, 503, 729
- Kim S., Dopita M. A., Staveley-Smith L., Bessell M. S., 1999, *AJ*, 118, 2797
- Kim S., Staveley-Smith L., Dopita M. A., Sault R. J., Lee Y., Chu Y.-H., 2002, *ApJ*, submitted
- Kroupa P., Bastian U., 1997, *New Astr.*, 2, 77
- Lang K. R., 1991, *Astrophysical Data: Planets and Stars*. Springer-Verlag, New York, p.103
- Li P. S., 1999, Ph.D. thesis. University of Wyoming
- Lu L., Sargent W. L. W., Savage B. D., Wakker B. P., Sembach K. R., Oosterloo T. A., 1998, *AJ*, 115, 162
- Luks Th., 1991, Ph.D. thesis. University of Bochum
- Luks Th., Rohlfs K., 1992, *A&A*, 263, 41 (LR92)
- Majewski S. R., Ostheimer J. C., Patterson R. J., Kunkel W. E., Johnston K. V., Geisler D., 2000, *AJ*, 119, 760
- McGee R. X., Haynes R. F., Groganard R. J.-M., Malin D., 1986, *MNRAS*, 221, 543
- McGee R. X., Milton J. A., 1966, *Australian J. Phys.*, 19, 343
- McGee R. X., Newton L. M., 1986, *PASA*, 6, 471
- Martínez-Delgado D., Alonso-García J., Aparicio A., Gómez-Flechoso M. A., 2001, *ApJ*, 549, 63
- Meaburn J., 1980, *MNRAS*, 192, 365
- Milgrom M., 1983, *ApJ*, 270, 365
- Mochizuki K., Nakagawa T., Doi Y., Yui Y. Y., Okuda H., Shibai H., Yui M., Nishimura T., Low F. J., 1994, *ApJ*, 430, 37
- Moore B., Davis M., 1994, *MNRAS*, 270, 209
- Murali C., 2000, *ApJ*, 529, 81
- Oestreich M. O., Gochermann J., Schmidt-Kaler T., 1995, *A&AS*, 112, 495
- Oey M. S., 1996, *ApJ*, 467, 666
- Oey M. S., Groves B., Staveley-Smith L., Smith R. C., 2002, *AJ*, 123, 255
- Olsen K. A., Kim S., Buss J. F., 2001, *AJ*, 121, 3075
- Padoan P., Kim S., Goodman A., Staveley-Smith L., 2001, *ApJ*, 555, 33
- Points S. D., Chu Y.-H., Kim S., Smith R. C., Snowden S. L., Brandner W., Gruendl R. A., 1999, *ApJ*, 518, 298
- Points S. D., Chu Y.-H., Snowden S. L., Staveley-Smith L., 2000, *ApJ*, 545, 827
- Putman M. E. et al., 1998, *Nature*, 394, 752
- Putman M. E., Staveley-Smith L., Freeman K. C., Gibson B. K., Barnes D. G., 2002, *ApJ*, in press
- Richter P., de Boer K. S., Widmann H., Kappelmann N., Gringel W., Grewing M., Barnstedt J., 1999, *Nature*, 402, 386
- Rohlfs K., Kreitschmann J., Siegman B. C., Feitzinger J. V., 1984, *A&A*, 137, 343
- Schlegel D. J., Finkbeiner D. P., Davis M., 1998, *ApJ*, 500, 525
- Schwering P. B. W., Israel F. P., 1991, *A&A*, 246, 231
- Stanimirović S., Staveley-Smith L., Dickey J. M., Sault R. J., Snowden S. L., 1999, *MNRAS*, 302, 417
- Staveley-Smith L., Kim S., Putman M., Stanimirovic S., 1998, *Rev. Mod. Astr.*, 11, 117
- Staveley-Smith L., Wilson W. E., Bird T. S., Disney M. J., Ekers R. D., Freeman K. C., Haynes R. F., Sinclair M. W., Vaile R. A., Webster, R. L., Wright A. E., 1996, *PASA*, 13, 243
- Swaters R., 1999, Ph.D. thesis. University of Groningen
- Tumlinson J., Shull J. M., Rachford B. L., Browning M. K., Snow T. P., Fullerton A. W., Jenkins E. B., Savage, B. D., Crowther P. A., Moos H. W., Sembach K. R., Sonneborn G., York D. G., 2002, *ApJ*, 566, 857
- van der Marel, R. P., 2001, *AJ*, 122, 1827
- van der Marel, R. P., Cioni, M.-R. L., 2001, *AJ*, 122, 1807
- Wada K., Spaans M., Kim S., 2000, *ApJ*, 540, 797
- Wakker B., Howk J. C., Chu Y.-H., Bomans D., Points S. D., 1998, *ApJ*, 499, L87
- Weaver R., McCray R., Castor J., Shapiro P., Moore R., 1977, *ApJ*, 218, 377
- Weinberg M. D., 2000, *ApJ*, 532, 922
- Weinberg M. D., Nikolaev S. 2001, *ApJ*, 548, 712
- Welch D. L., McLaren R. A., Madore B. F., McAlary C. W., 1987, *ApJ*, 321, 162
- Westerlund B. E., Mathewson D. S., 1966, *MNRAS*, 131, 371
- Williams D. R. W., 1973, *A&AS*, 8, 505
- Zaritsky D., 1999, *AJ*, 118, 2842
- Zaritsky D., Lin D. N. C., 1997, *AJ*, 114, 2545